DESIGN OF OPTOMECHANICAL SENSING DEVICES BASED ON AL_2O_3 PLATFORMS

Master Thesis

Safiye YÜCEL

Eskişehir, 2023

DESIGN OF OPTOMECHANICAL SENSING DEVICES BASED ON AL2O3 PLATFORM

Safiye YÜCEL

Master's Thesis

Department of Electrical-Electronics Engineering

Programme in Electromagnetics Field and Microwave Circuits

Supervisor: Prof. Dr. Feridun AY

Eskişehir

Eskişehir Technical University

Institute of Graduate Programs

January 2023

FINAL APPROVAL FOR THESIS

This thesis titled DESIGN OF OPTOMECHANICAL SENSING DEVICES BASED ON AL2O3 PLATFORM has been prepared and submitted by Safiye YÜCEL in partial fulfillment of the requirements in "Eskişehir Technical University Directive on Graduate Education and Examination" for the Degree of Master's in Electrical-Electronics Engineering Department has been examined and approved on 17/01/2023.

Committee Members		Title, Name and Surname	Signature
Member	:	Prof. Dr. Feridun AY	
Member	:	Prof. Dr. Nihan KOSKU PERKGÖZ	
Member	:	Doç. Dr. Hayrettin ODABAŞI	

Prof. Dr. Murat TANIŞLI
Director of the Institute of Graduate Programs

17/01/2023

SUPERVISOR APPROVAL

Master's student Safiye YÜCEL, whom I supervise, has completed this thesis titled DESIGN OF OPTOMECHANICAL SENSING DEVICES BASED ON AL2O3 PLATFORM. According to my inspections, the work is scientifically and ethically appropriate for the student to the thesis defense exam.

Supervisor
Prof. Dr. Feridun AY

ABSTRACT

DESIGN OF OPTOMECHANICAL SENSING DEVICES BASED ON AL2O3 PLATFORM

Safiye YÜCEL

Department of Electrical-Electronics Engineering

Programme in Electromagnetics Field and Microwave Circuits

Eskişehir Technical University, Institute of Graduate Programs, January 2023

Supervisor: Prof. Dr. Feridun AY

Light has been used for a very long time. As a result, equipment with principles of operation based on the transmission and reflection of light has been created.

In this paper, integrated ring resonator-based sensors are the main subject of design and analytical studies. Like standard MEMS in operation, studying MOEMS structures produces superior results in key areas including sensitivity, noise, and shock value. A single-mode ridge waveguide geometry and an Al_2O_3-based ring resonator form the designed devices. Superior features like a high refractive index, rare earth ion doping, high light confinement, minimal loss, stability, transparency, and adaptability to optical fibers are provided by Al_2O_3 for the integrated circuit. The MOEMS accelerometer can be created using a ring resonator device formed of Al_2O_3. The system is based on the theory that the cantilever structure's acceleration-induced bending changes the ring resonator's refractive index, affecting the wavelength shift's measurement.

Analyses of the designed accelerometer's optics and mechanics were performed. This optimization research used numerical techniques like FDTD and FEM. The parameters collected as a consequence of the analysis were used to improve the device. The study has revealed that a more sensitive accelerometer that is also less expensive and has high sensitivity and a low noise ratio than those on the market has been created.

Keywords: Micro-Ring Resonator, MOEMS, Accelerometer Sensor, Al2O3, Waveguide.

ÖZET

OPTOMEKANIK ALGILAMA CIHAZLARININ AL2O3 TABANLI PLATFORMLARDA DIZAYNI

Safiye YÜCEL

Elektrik-Elektronik Mühendisliği Anabilim Dalı

Elektromanyetik Alanlar ve Mikrodalga Tekniği Bilim Dalı

Eskişehir Teknik Üniversitesi, Lisansüstü Eğitim Enstitüsü, Ocak 2023

Danışman: Prof. Dr. Feridun AY

Işık çok uzun süredir hayatımızda yer almaktadır. Sonuç olarak, ışığın iletilmesi ve yansımasına dayalı çalışma prensibine sahip cihazlar icat edilmiştir.

Bu çalışmada entegre halka rezonatör tabanlı sensörlerin, tasarımı ve analitik hesaplamaları ana konuyu oluşturmaktadır. Kullanımdaki standart MEMS'e benzer şekilde, MOEMS yapıları incelendiğinde hassasiyet, gürültü ve şok değeri gibi kilit alanlarda üstün sonuçlar verir. Tasarlanan cihazları oluşturmak için Al_2O_3 tabanlı tek modlu bir sırt dalga kılavuzu geometrisi ve bir halka rezonatör kullanılmıştır. Entegre devre için yüksek kırılma indeksi, nadir toprak iyon katkısı, yüksek ışık yakalama, minimum kayıp, kararlılık, şeffaflık ve optik fiberlere uyarlanabilirlik gibi üstün özellikler Al_2O_3 tarafından sağlanmaktadır. MOEMS ivmeölçeri, Al_2O_3'ten oluşan bir halka rezonatör kullanılarak oluşturulabilir. Sistem, konsol yapısının ivme kaynaklı bükülmesinin, halka rezonatörün kırılma indeksini değiştirip, dalga boyu kaymasının ölçümü teorisine dayanmaktadır.

Tasarlanan ivme ölçerin optik ve mekanik analizleri yapılmıştır. Bu optimizasyon araştırmasında FDTD ve FEM gibi sayısal teknikler kullanıldı. Analiz sonucunda toplanan parametreler cihazın iyileştirilmesinde kullanılmıştır. Çalışma, piyasadakilerden daha hassas, aynı zamanda daha ucuz, darbe direnci daha yüksek ve gürültü oranı düşük bir ivmeölçer tasarlandığını ortaya koydu.

Anahtar Sözcükler: Mikro Halka Rezonatör, MOEMS, İvme Sensörü, Al2O3, Dalga Kılavuzu.

ACKNOWLEDGEMENTS

I would like to thank my advisor Prof. Dr. Feridun Ay for his continuous encouragement during this work with his supportive attitude, his spare time under all circumstances, his patience, energy, and experience, enlightening my path, making sure that I move forward on this path and making this difficult journey enjoyable. Again, I would like to thank Prof. Dr. Nihan Kosku Perkgöz, who never spared her interest, knowledge, time, and smiling face.

I would like to thank my MIDAS colleagues, who supported me in my studies and provided me with a good working environment during this process, for making this process easier and enjoyable.

Finally, I would like to express my biggest thanks to my family. I owe everything to their endless support, love, and trust. With their encouraging attitudes, I learned not to give up, to overcome the obstacles in my way, and to succeed. For this reason, I devote this work to my father Tayfun Yücel, my mother Şükran Yücel, and my sister Nafiye Dilber Yücel.

Safiye YÜCEL

17/01/2023

STATEMENT OF COMPLIANCE WITH ETHICAL PRINCIPLES AND RULES

I hereby truthfully declare that this thesis is an original work prepared by me; that I have behaved in accordance with the scientific ethical principles and rules throughout the stages of preparation, data collection, analysis and presentation of my work; that I have cited the sources of all the data and information that could be obtained within the scope of this study, and included these sources in the references section; and that this study has been scanned for plagiarism with "scientific plagiarism detection program" used by Eskişehir Technical University, and that "it does not have any plagiarism" whatsoever. I also declare that, if a case contrary to my declaration is detected in my work at any time, I hereby express my consent to all the ethical and legal consequences that are involved.

Safiye YÜCEL

CONTENTS

Page

LIST OF TABLES

Page

LIST OF FIGURES

Page

GLOSSARY OF SYMBOLS AND ABBREVIATIONS

E_{r1}	:	Coupled Energy with Ring Resonator
κ	:	Coupling Coefficient
n_{eff}	:	Effective Refractive Index
E_{r2}	:	Energy Circulating Around the Ring Resonator
n_g	:	Group Index
E_{in}	:	Incident Wave Energy
A	:	Loss Coefficient
L	:	Ring Resonator Perimeter
R	:	Ring Radius
T	:	Transmission Coefficient
E_{out}	:	Transmission Wave Energy
Λ	:	Wavelength
2D	:	2-Dimensional
3D	:	3-Dimensional
AlGaAs	:	Aluminium Gallium Arsenide
Al_2O_3	:	Aluminum Oxide
ALD	:	Atomic Layer Deposition
CCD	:	Charge-Coupled Devices
CVD	:	Chemical Vapor Deposition
Cr	:	Chromium
Er^{3+}	:	Erbium Ion
ER	:	Extinction Ratio
F	:	Finesse
FDE	:	Finite Different Eigenmode
FDTD	:	Finite-Different Time-Domain
FEM	:	Finite Element Method
FSR	:	Free Spectral Range
FWHM	:	Full Width at Half Maximum
Ho^{3+}	:	Holmium Ion
InGaAsP/InP	:	Indium Gallium Arsenide Phosphide/Indium Phosphide

IR	:	Infrared
IC	:	Integrated Circuit
Laser	:	Light Amplification by Stimulated Emission of Radiation
LED	:	Light Emitting Diode
$LiNbO_3$	:	Lithium Niobate
MEMS	:	Micro Electro Mechanical Systems
MOEMS	:	Micro Opto Electro Mechanical Systems
MMI	:	Multimode Interference
Nd^{3+}	:	Neodymium Ion
PEC	:	Perfect Electric Conductor
PML	:	Perfectly Matched Layer
Q	:	Quality Factor
RIU	:	Refractive Index Units
SiO_2	:	Silicon Dioxide
SOI	:	Silicon on Insulator
Tm^{3+}	:	Thulium Ion
TE Mode	:	Transverse Electric Mode
TEM Mode	:	Transverse Electromagnetic Mode
TM Mode	:	Transverse Magnetic Mode
UV	:	Ultraviolet
WDM	:	Wavelength-Division Multiplexing
Yb^{3+}	:	Ytterbium Ion

1. INTRODUCTION

1.1. Integrated Optical Devices From Past To Present

The necessity of communication, data transfer from one place to another, and sensing technologies is an ever-increasing need that has existed since human beings. These are necessary for people to interact with each other and their environment, that is, to conduct their lives healthily. The methods used for these needs have developed from the past to the present and have gained diversity (Pollock & Lipson, 2003). Undoubtedly, the most efficient of these methods and always the focus of research are those related to light (Kikuchi, 2010).

Optics is a science that covers a wide period from the discovery of fire to the invention of lasers and continues to develop today (Chang, 2005). It covers studies involving the detection and control of photons (Ohtsu, Kobayashi, Kawazoe, Yatsui, & Naruse, 2007). These systems have many advantages compared to other methods due to the unique properties of photons. High sensitivity, high speed, wide bandwidth, low dimensions, low noise, electromagnetic sensitivity, and resistance to electrical interference can be examples of these advantages (De & Sen, 2011). Despite its disadvantages, such as complex structure and high cost, its positive aspects predominate, and it is used extensively in many areas today (Selvarajan, 1992).

The science of optoelectronics is formed by the combination of systems that detect, transmit, and manage light with electronic circuit elements (Kumar & Patel, 1992). In these systems, conversions between electrical energy and light energy are applied according to the area and purpose of use (Piprek, 2017). When grouped as light emission and light detection, the light emission group, which has examples such as light-emitting diode (LED) and light amplification by stimulated emission of radiation (laser), converts electrical energy into light energy. Circuit elements such as photodiodes and solar cells in the light detection group convert light energy into electrical energy. (DiLoui, 2008). These two working principles can be found in a single circuit. These circuits, which consist of more than one circuit element, are called IC (integrated circuits). These structures, called chip technology, appear in many areas of life with features such as high sensitivity, low noise, small size, and low production costs (Iwai & Ohmi, 2002). It is possible to see simple LED applications such as traffic lights (Pathak et al., 2015)and complex applications such as the Charge-Coupled Devices (CCD) used in the Hubble Space Telescope(*NASA*, 2022) in many areas from the health field to the energy sector, from space applications to the defense industry, from daily life to the entertainment sector, from communication to data storage. For example, new micro-satellites are produced with the small dimensions of CCD, superior image processing quality, and durability in harsh environmental conditions. These small satellites reduce the cost considerably and provide ease of application (X. Chen et al., 2007). As Moore's law states, the number of circuit elements placed on an integrated circuit doubles every two years (Schaller, 1997). This law proves that integrated circuits will become smaller but more complex structures. This demonstrates the necessity and importance of nanotechnology studies.

The superior properties of light provide many benefits in the field of technology. For example, it can carry more data because it has a higher frequency than the radio wave (Dianov, 2010). Considering the era's intense data transfer and communication needs, this feature is essential. However, more than such features are required. To use these features, the energy of the light must be transported from one place to another without being loss (Ay, 2005). For this process, waveguides, an integrated circuit element that forms the basis of this study, are used (Il'inskii, 2019). Light, an electromagnetic wave, travels in its free state by weakening according to the inverse square law (Vera et al., 2014). However, waveguides aim to minimize energy loss by restricting the transmission in one direction (Kogelnik, 1988). There are varieties according to geometry and usage area. Radiofrequency waveguides, acoustic waveguides, and optics waveguides are examples of their types according to their application areas. In this study, studies were carried out on optical waveguides. In addition, waveguides have various geometries such as rectangular, circular, elliptical, stripped, buried, rib, and ridge.

1.2. Optomechanical Systems

Optomechanics is a set of systems for holding, aligning, and turning optical elements into sensors (Schwertz & Burge, 1988). Optomechanical design and analysis cover an extensive area. Motion and orientation, material analysis, position determining, mounting of optical components, and tolerance evaluation are some steps of this process (Yoder P, 1992.). More specifically, in optomechanics, mechanical vibrations, typically micro or nanometer scale resonators, are controlled by laser light. In this study, intensive work has been done on this subject. The optical and mechanical design and analysis of the optomechanical system were made. After that, these two structures were combined, and the optomechanical analyzes were completed. These three titles are required to design devices with optical working principles that include mechanical movement, such as the accelerometer sensor studied in the thesis. Micro-Opto-electro-mechanical Systems (MOEMS), which have similar working principles to Micro-electro-mechanical Systems (MEMS) structures, work according to optical principles. It is seen in Figure 1.1 that it is an interdisciplinary system.

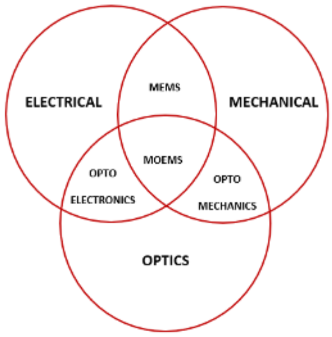

Figure 1.1. *The branches of science included in MOEMS*

MOEMS systems are more sensitive and have fewer limits than conventional MEMS. A comparison of some parameters of MOEMS and MEMS structures is given in Table 1.1. In this study, microring resonators were used. Ring resonators can be used as displacement sensors (Liu et al., 2009), temperature sensors (Singha & Bhowmik, 2018), surface detection sensors (Kim & Fan, 2015), and biosensors (Kianisarkaleh et al., 2017).

Table 1.1. *Comparison of essential parameters of MOEMS and MEMS systems*

Parameter	MOEMS	MEMS
Sensitivity	5V/g	1.2 V/g
Working Range	0.001-2000g	1-2500g
Bandwidth	0-1000 Hz	0-1500 Hz
Noise	10 $\mu gHz^{-1/2}$	140 $\mu gHz^{-1/2}$
Shock Value	5000 g	6000 g

In this study, MOEMS accelerometers were studied. High sensitivity and low optical losses have been achieved compared with similar structures. The quality factor (Q) is an important parameter in determining the sensitivity of ring resonators. 1.3 x10^4 (Dong et al., 2013), 3.3 x10^4 (Kwon & Steier, 2008b), and 1.4 x10^4 (Y. Chen et al., 2009) can be given as examples of Q values of structures similar to those in the study. The value found in the study is 5.02 x10^5. As a result, sharper resonant wavelengths were obtained. This increases the accuracy and intensity of the measurement.

1.3. Why Al_2O_3-Based Devices?

The materials that fabricate the waveguide also give variety according to the usage area and geometry. Dielectrics such as SiO_2, $LiNbO_3$, InGaAsP/InP, AlGaAs, Al_2O_3(Demirtas et al., 2018), conductors such as SOI, (Y. Li et al., 2015) and materials such as polymers (Chiang, 2010) are used in optical waveguide design.

Al_2O_3 is the most innovative of these materials. In this study, the designs made on this platform are included. There are two forms of Al_2O_3 as amorphous and crystalline. In this study, the amorphous form will be used. Al_2O_3 can be easily grown on SiO_2 wafers by the Atomic Layer Deposition (ALD) method. Due to its structure, it allows wafer-scale processing and monolithic integration (Goede, 2020). Compared to fabrication methods such as Chemical Vapor Deposition (CVD), the ALD method is more controlled in terms of material thickness and doping rate. Moreover, it is more affordable in terms of cost.

It can also be doped with rare earth ions such as Erbium, and Ytterbium (Bonneville et al., 2020). Compared to silicon-based photonic material platforms and silica-based glass, rare-earth ion doped Al_2O_3, has a substantially higher trivalent rare-earth ion solubility (J. D. B. Bradley et al., 2007). At several wavelengths, including 0.88 µm, 1.06 µm, and 1.33 µm for Nd^{3+} : Al_2O_3 (J. D. B. Bradley et al., 2014), 0.103 µm for Yb^{3+} : Al_2O_3, 1.55 µm for Er^{3+} : Al_2O_3, 1.8 µm -1.9 µm for Tm^{3+} : Al_2O_3(Su et al., 2016), and 2 µm for Ho^{3+} : Al_2O_3(N. Li et al., 2018), rare-earth ion doping was demonstrated for active operation. Modern laser technologies were founded on the lasing activity in Cr-doped Al_2O_3 (Hadi Kusuma et al., 2009).

In addition, Al_2O_3 is a material with excellent physical, chemical, and thermal stability (Edlmayr et al., 2010). As a result of these properties, active devices can be created. Amplifiers and lasers are active devices. Resonators, couplers, multiplexers, optical filters, and power dividers can be passive devices made of pure material.

It works not only at visible wavelengths but also at infrared (IR) and ultraviolet (UV) wavelengths with its transparency feature (L. Zhang et al., 2014). In the optical transmission from the UV to IR spectrum, pure Al_2O_3 is a strong material. It has been determined that it provides transparent windows between 150 nm and 5500 nm (Yang & Guo, 2006). Its transparency feature shows thermal stability. For example, no change was observed in the percentage of transparency in annealing at 300 ºC, 500 ºC, 600 ºC, 700 ºC, and 800 ºC (Q. Y. Zhang et al., 2000).

Optical losses are minimal. A propagation loss of 0.23 dB/cm has been reported (Arnold & Cole, 1988). A waveguide fabricated by the ALD method reports 0.04+0.02 dB/cm (N. Li et al., 2018). Low losses at wide wavelengths allow different sensor applications. An example is the biosensor study that detects cancer cells (de Goede et al., 2019).

Its refractive index difference increases the sensitivity in sensor applications such as SiO_2 used as cladding. Refractive index differences allow the light to travel slowly in the waveguide. It prevents the scattering of the wave and restricts the wave in one direction. As a result, loss values are reduced (Caballero-Espitia et al., 2020).

1.4. Outline Of Thesis

The aim of the study is the design of MOEMS systems using waveguides. While creating these systems, an innovative material, Al_2O_3, was used, and ring resonators were designed from simulated waveguides. Afterward, a detection system was fabricated from this structure.

Detection systems can be created using integrated circuits. The general name of these systems is sensors. Sensors detect environmental changes and generate an output according to the detected parameter. These parameters can be inputs such as motion, temperature, humidity, light, or pressure.

In Chapter 2 of this study, an accelerometer was designed using the ring resonator structure. The mechanical simulations required for the optomechanical sensor were made, and the results were analyzed.

The working principle, types, and application areas of waveguides are discussed in Chapter 3. The focus is on optical waveguides, which form the basis of the study. The necessary information for the analysis of ridge waveguides operating as single mode based on Al_2O_3 and simulation results can be examined in this section.

In Chapter 4, ring resonators are discussed. The general applications and types of ring resonators are mentioned, and then the Al_2O_3-based ring resonator structure is mentioned. After explaining the theoretical calculations for the single-ring resonator, simulation studies are shown. The necessary steps for simulation and simulation results are also in this section.

2. AL_2O_3 RING RESONATOR BASED MOEMS

MOEMS systems consist of a combination of optical, electrical, and mechanical fields. MOEMS has recently become highly preferred in device designs with its increased sensitivity, low noise ratio, small dimensions, and low cost. It has a wide application area with usage areas such as Tunable Lasers, Wavelength-division multiplexing (WDM), Digital Mirror Devices, and Scanners (Mounier et al., 2006). In this study, a sensing system, that is, a sensor, was designed from the ring resonator whose dimensions were decided as a result of simulation and theoretical calculations. Dimensions and materials specified in the following sections will be used in the system. An accelerometer sensor was created with the designed ring resonator.

2.1. Moems Accelerometer

It is planned to make an accelerometer using the designed integrated optical circuit. The working principle of this accelerometer is to measure the shift in wavelength. The ring resonator is placed on top of a cantilever with the ring suspended. The cantilever structure bends when a force is applied to the device or gains speed. Therefore, the ring is bent in the resonator. This bending causes the wavelength to shift. When this shift value is measured, the accelerometer operating principle is completed, and the varying acceleration can thus be measured. A draft prototype of the designed device is shown in Figure 2.1

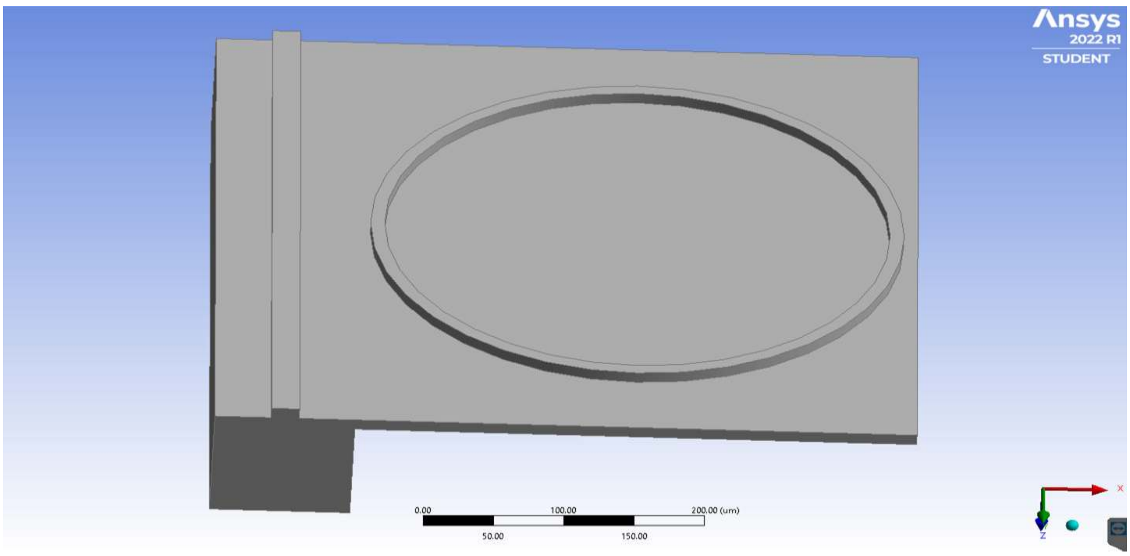

Figure 2.1. *Prototype of the ring resonator accelerometer*

2.1.1. Mechanical simulations

Mechanical simulations are made to understand the effect of bending on wavelength. The Finite Element Method (FEM) was used in simulations. Ansys Workbench and Ansys Mechanical modules were used for simulations.

2.1.1.1. Preparation for simulation

There are two critical points in the simulations using the FEM method. The first of these is the boundary conditions. Boundary conditions can be given features such as fixed support and applied force. The more accurately these are set, the closer the results will be to reality. For example, fixed support allows the object to move and prevents the object from moving only in the specified axis. In contrast, frictionless support prevents the object from moving in all axes. The second is the meshing part of the object. An incorrect mesh will make the simulation results directly wrong. Ansys Mechanical uses tetrahedral element meshing and hexahedral element meshing methods in 3D mesh shapes. These mesh methods should be chosen according to the geometry of the object and the simulation purpose and time. When necessary, a hybrid mesh structure can be created using both together. In this study, the hexahedral mesh method was used. An example of the Ansys Mechanical module is shown in Figure 2.2.

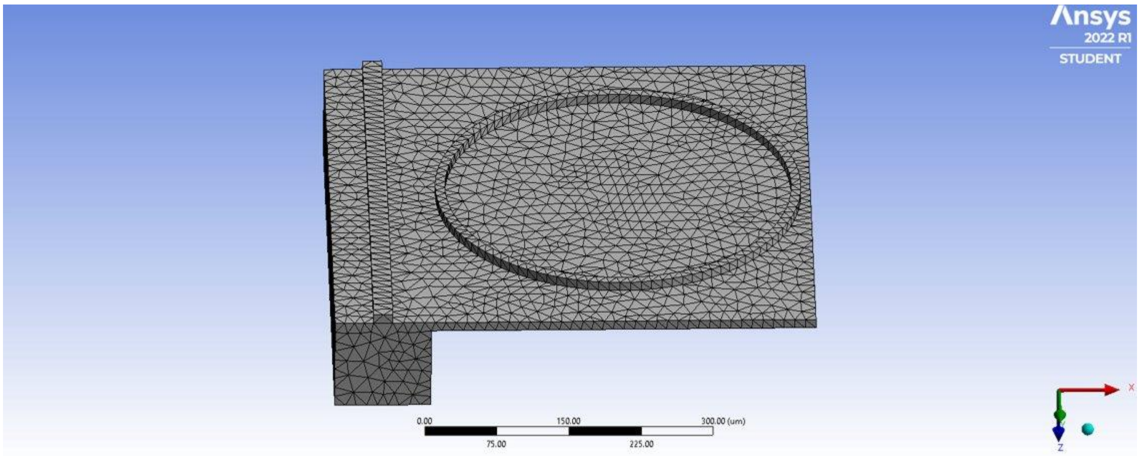

Figure 2.2. *Hexahedral mesh structure from Ansys Mechanical*

Other necessary boundary conditions are then set. Two surface support, frictionless and fixed, were used in the simulation. In turn, one fixes completely, and the other allows shifting in undefined axes. These choices were made to increase accuracy and get the same results in life. Examples of supports applied to surfaces are shown in Figure 2.3.a and Figure 2.3.b. The first is fixed support; the second is frictionless support. A force is applied to the place where the ring resonator is located. (Figure 2.4.a)

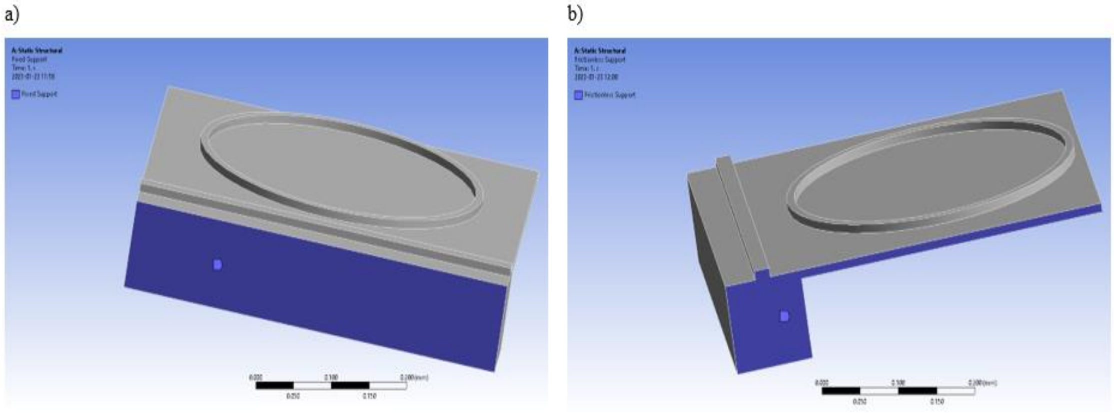

Figure 2.3. *Fixed support (a), frictionless support (b) applied to different surfaces in the simulation*

2.1.1.2. Simulation results

The analysis is started by adding the desired results from the simulation. As a result of the simulation, the top view of the stress distribution is as in Figure 2.4.b. Top and side views showing the total deformation rates are as in Figure 2.4.c and Figure 2.4.d, respectively. The color distribution gives a value scale, as can be seen from the bar next to it. Whichever value is being examined, red takes the highest and blue the lowest. It can be defined and changed depending on the user. For example, the most intense region in the stress distribution is where the red colors are and the cantilever is bent. The farthest section of the cantilever and its fixed region correspond to the area with minimal stress distribution, visually indicated by the color blue. In the results of the deformation simulation, conversely, the farthest point, experiencing the maximum deformation due to bending, is indicated by the color red. When observed from a lateral perspective, the black guide lines depicted in Figure 2.4.d exemplify the unaltered condition of the cantilever within the context of the deformation simulation findings. Consequently, it becomes feasible to discern the magnitude of deflection.

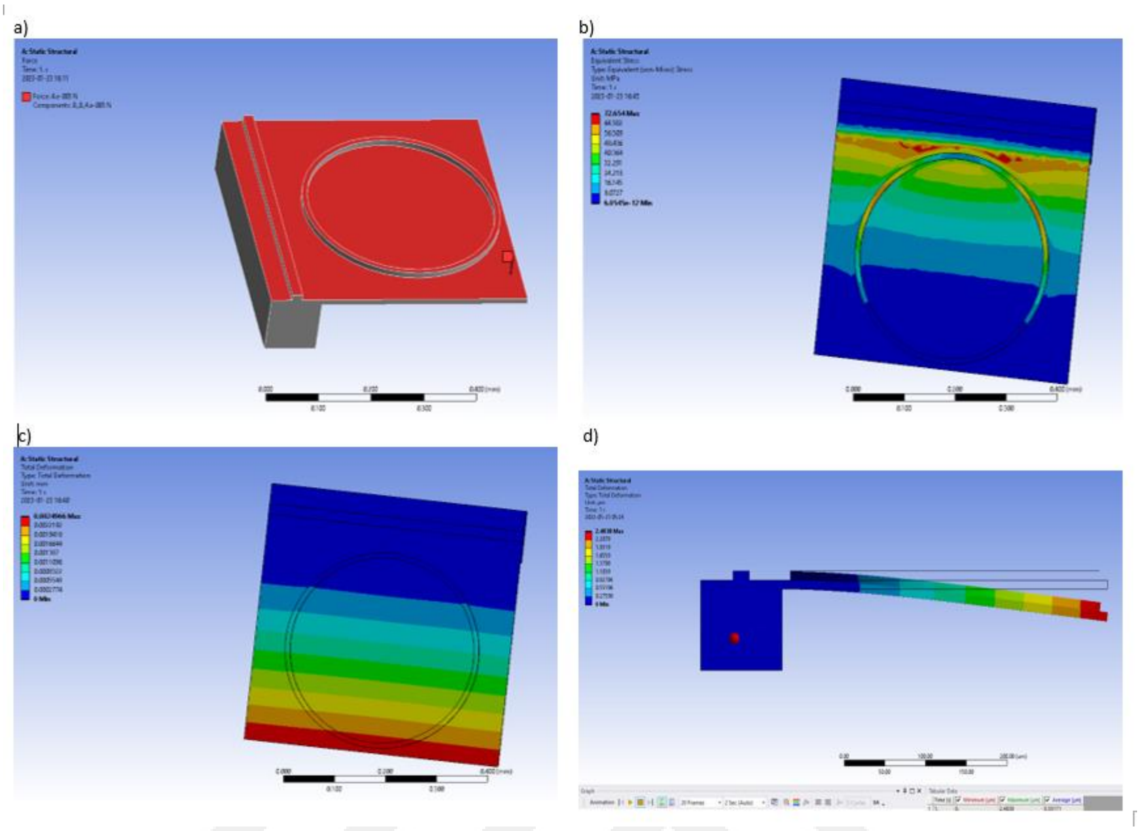

Figure 2.4. *Applied force for acceleration (a). Stress distribution of top view (b). Total deformation of top view (c) and side view (d)*

Every substance has a natural frequency. It makes a continuous oscillation without external force. The value at which this oscillation is maximum is called the resonant frequency. The oscillations will increase if the external force applied to the object is equivalent to the resonant frequency. The result is that the object is strained or fractured. It is essential to detect natural frequencies, especially in device production, to prevent this situation. The frequencies and oscillation patterns of the first six modes were found using Ansys Mechanical for the designed device. The second and third modes are presented in Figure 2.5, illustrating their individualized oscillatory characteristics. For instance, the first mode is characterized by a bending motion. In the second mode, the right and left ends move in an upward and downward manner, respectively. In the third mode, the central portion undergoes vertical displacement.

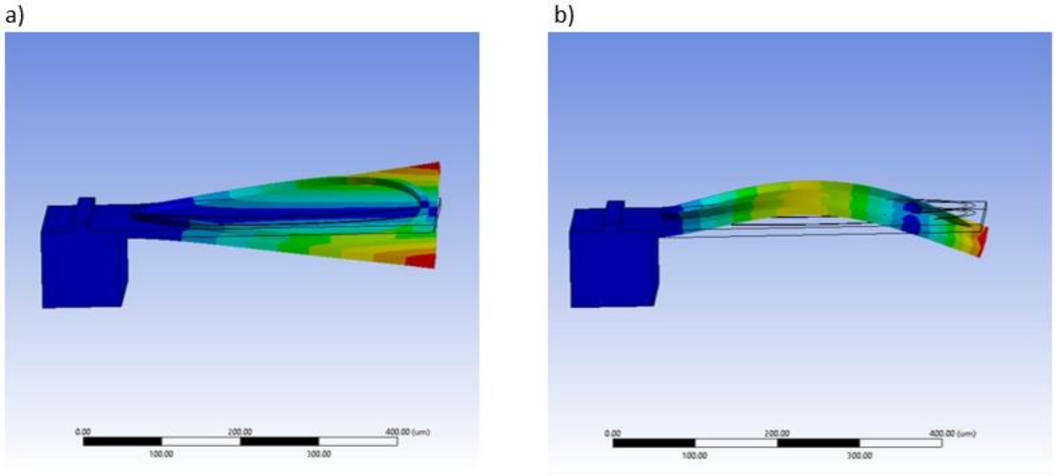

Figure 2.5. *Resonance frequency analysis. The first figure represents the 2nd mode. It consists of the up and down movement of the right and left ends of the cantilever, respectively. (a) The other figure represents the 3rd mode. It consists of stretching and flattening the cantilever's middle part by bending it from the front end. (b).*

When acceleration was applied to the device, the effective index changed by 0.1084. This result caused a shift of approximately 0.982 nm in the transmission spectrum (Figure 2.6). Optical sensitivity was found to be 905 nm/RIU.

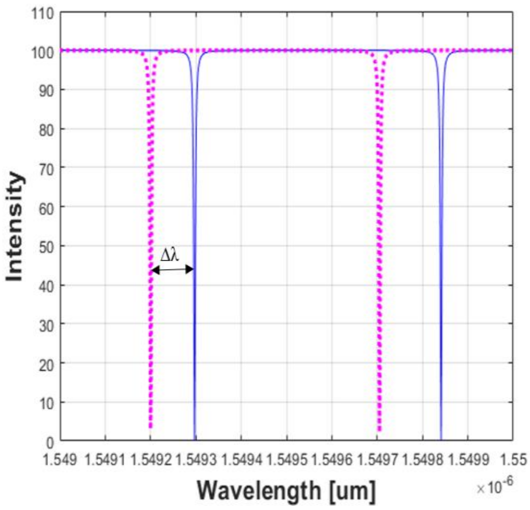

Figure 2.6. *Change in transmission spectrum due to acceleration*

The solid blue line is the non-accelerated state, and the dotted pink line is the accelerated transmission spectrum. By measuring this shift value, the working principle of the accelerometer is obtained. The amount of shift in the wavelength according to the applied force and the movement of the cantilever is given in Figure 2.7.

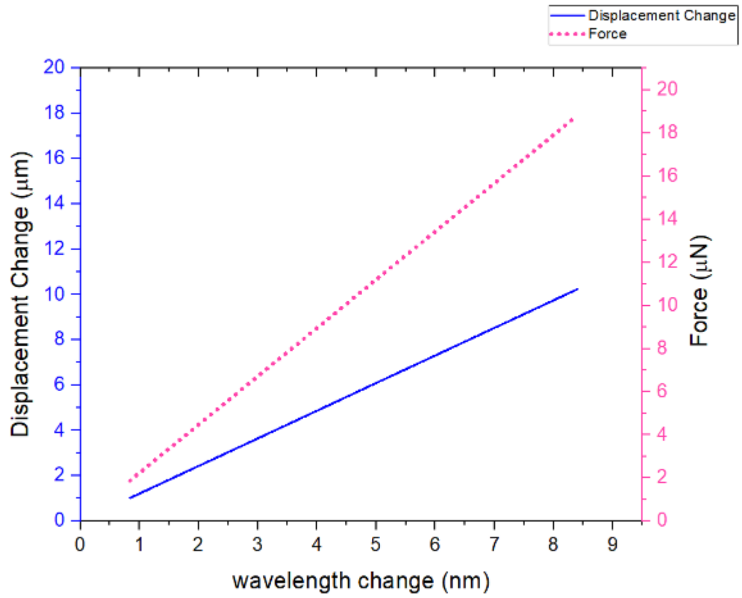

Figure 2.7. *Relationship of wavelength shift in transmission spectrum with applied force and motion of the cantilever*

As a result, a graph of wavelength shift and acceleration change was obtained with the data taken from the simulations for the intended use of the designed device (Figure 2.8). Mechanical sensitivity was found to be 0.11 nm/g.

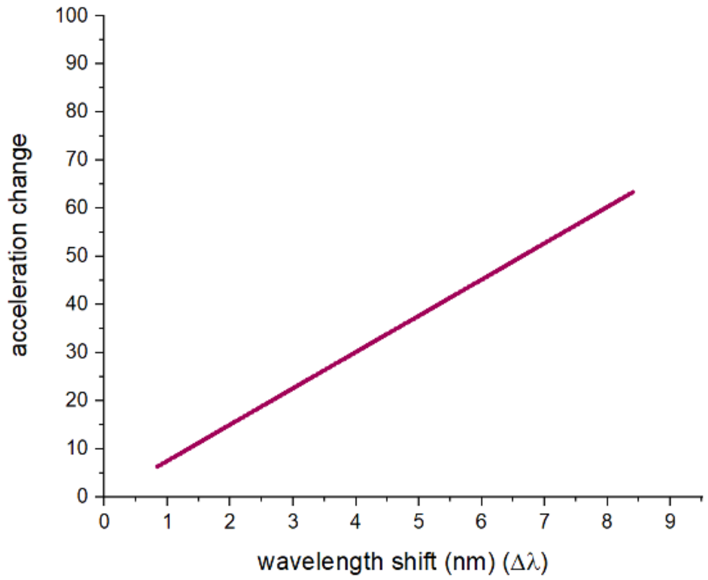

Figure 2.8. *The measured acceleration change due to the wavelength shift in the transmission spectrum*

3. WAVEGUIDES

Waveguides are various according to their usage areas and purposes. It differs in shape, such as a planar waveguide, circular waveguide, or ridge waveguide, or in terms of working principles, such as a step-index waveguide and single mode waveguide. Figure 3.1 presents some examples of waveguide types(Bhandarkar, 2005). Its purpose is to propagate a wave in the desired direction with a minimum loss, as mentioned in the introduction. The wave transmission is a mode inside the waveguide. These modes depend on the cross-sectional area of the waveguide, its material, and many other parameters. There are three kinds of wave modes.

Transverse Electric (TE) Modes: The electric field is perpendicular to the direction of propagation. They are also called H modes because there is only a magnetic field in the propagation direction.

Transverse Magnetic (TM) Modes: The magnetic field is perpendicular to the direction of propagation. They are also called E modes because there is only an electric field in the direction of propagation.

Transverse Electromagnetic (TEM) Modes: The electric and magnetic fields are perpendicular to the direction of propagation.

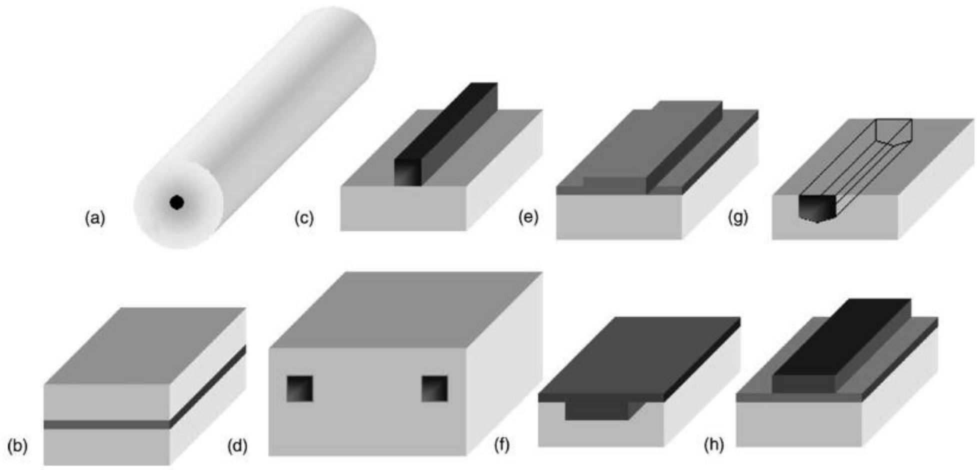

Figure 3.1. *Waveguide structure examples (a) Optical fiber (b) Slab waveguide (c) Channel waveguide (d) Embedded channel waveguide (e) rib waveguide (f) inverted rib waveguide (g) ıon diffused (h) strip waveguide*

The waveguide designed in the thesis is required to operate as a single mode. This condition exists only if the waveguide supports only one TE mode, one TM mode, or one

TE mode and one TM mode. Regardless of the purpose, wave modes must fully support the desired mode and completely prevent undesired modes.

3.1. Optical Waveguides

In both local and long-distance optical communication systems, optical waveguides are utilized as the transmission medium or as parts of integrated optical circuits (Ramo, 1994). A spatially inhomogeneous device known as an optical waveguide is used to direct light and limit the space in which light can flow. A waveguide typically has an area with a higher refractive index than the surrounding medium called cladding. The region with a high refractive index is the core, and the region with refractive index contrast is the substrate. In this study, the core is Al_2O_3, substrate SiO_2, and cladding air.

3.2. Design Of Ridge Waveguide Based On Al_2O_3

This study studied a ridge waveguide structure using Al_2O_3 thin film. Two materials were used in the construction. SiO_2 substrate and Al_2O_3 were used as core layers. The high refractive index difference between SiO_2 and Al_2O_3 reduces losses and increases the waveguide's efficiency. The refractive index of SiO_2 is 1.44, and the refractive index of Al_2O_3 is approximately 1.64 at a wavelength of 1.55 micrometers, which is used in the simulation. To increase the accuracy of the simulation results, the refractive index of the Al_2O_3 thin film fabricated by the ALD method in the laboratory was measured with a Metricon 2010/M model prism coupler (Demirtas et al., 2018). Prism coupler is a measuring device using a light source and a prism. It transmits the laser light sent at the desired wavelength to the prism by passing it through the optical setup with some mirrors. Refractive index, thickness, or supported modes can be found by measuring the coupling between the light passing through the prism and the sample (F.Chen et al., 2019). The imaginary part of the refractive index was accepted as zero in the measured values. The values obtained as a result of the measurement are shown in Table 3.1.

While designing the waveguide, the sidewall angles were not chosen as 90°. This is because research indicates that the angles in fabrication are between 56° and 68° (Jonathan D. B. Bradley & Ipskamp, 2009). The side walls were at about 50 degrees in the fabrication carried out in clean room conditions in the laboratory (Kwon & Steier, 2008a). To increase the accuracy ratio in the simulation results, the side walls of the waveguide were chosen at 50°. The side walls are not 90° because it is impossible to etch the material at a right angle during the etching process.

Table 3.1. *Measured refractive index values of Al_2O_3 thin film between 1480 nm and 1550 nm wavelength*

Wavelength (nm)	Effective Refractive Index (Reel Part)	Effective Refractive Index (Imaginary Part)
1450	1.64085	0
1460	1.6408	0
1480	1.6407	0
1500	1.6406	0
1520	1.6405	0
1540	1.6405	0
1560	1.6404	0
1580	1.6403	0

The cross-section of the designed waveguide is shown in Figure 3.2. The upper layer represents Al_2O_3, and the lower layer represents SiO_2. In the following parts of the study, the total thickness of the waveguide will be denoted by t, the etch depth, that is, the core thickness e, and the width of the waveguide will be indicated by w. The purple layer represents Al_2O_3, and the gray layer represents SiO_2.

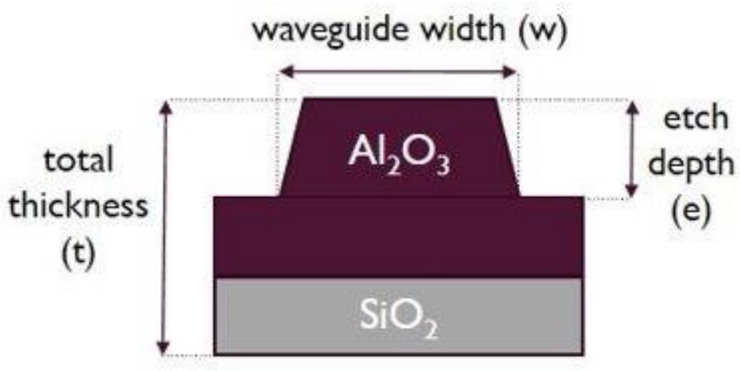

Figure 3.2. *Al_2O_3-based ridge waveguide cross-section. The purple parts represent Al_2O_3, and the gray represents the SiO_2 substrate.*

3.2.1. Simulation of the waveguide

3.2.1.1. Preparations for simulation

Ansys Lumerical software was used to design the waveguide. The simulation parameters have been determined to be compatible with real life. As mentioned in the previous section, the waveguide must operate in a single mode. Simulation studies were carried out to prevent fabrication errors and to determine the safe region. During these studies, the Mode module of Lumerical was used. (Figure 3.3)

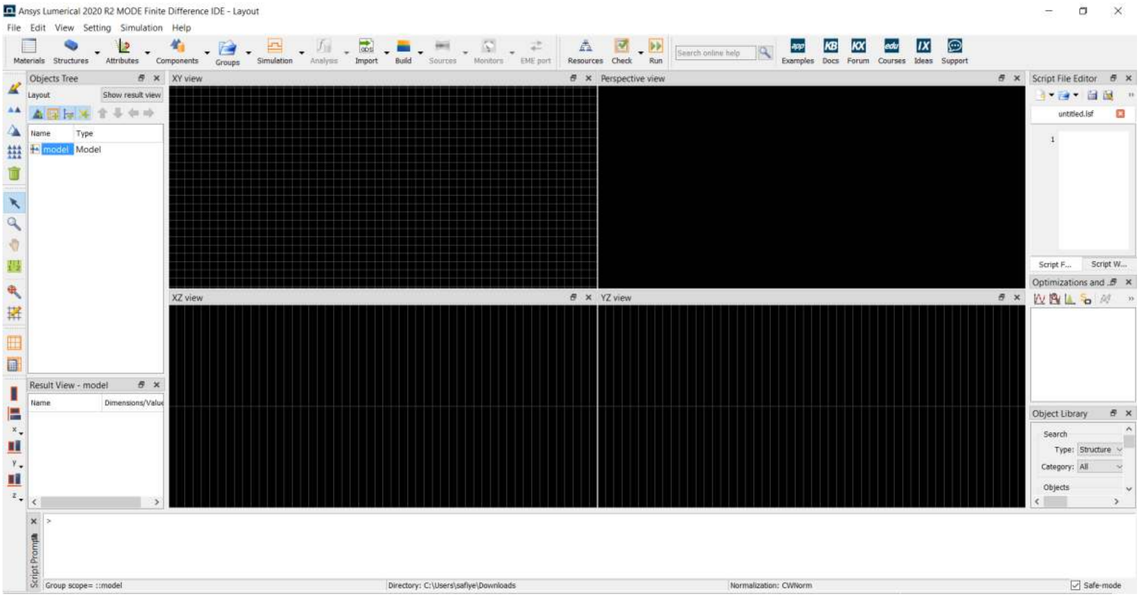

Figure 3.3. *Image of the interface of Ansys Lumerical 2020 R2 version*

Lumerical has a library of materials for simulation (Figure 3.4). However, the measurement results of Al_2O_3 produced in our laboratory, which was mentioned before, were used to obtain more realistic results. The software of the Lumerical program makes it possible to add external materials to the material library. It offers many options for choosing a suitable material for simulation. Sampled 3D data is ideal for this study from various materials such as (n,k) material, conductor 2D material, dielectric, perfect electric conductor (PEC), and plasma. A file containing the result of the measurements can be added by exporting it to the library. The name and color of the added material can be chosen optionally.

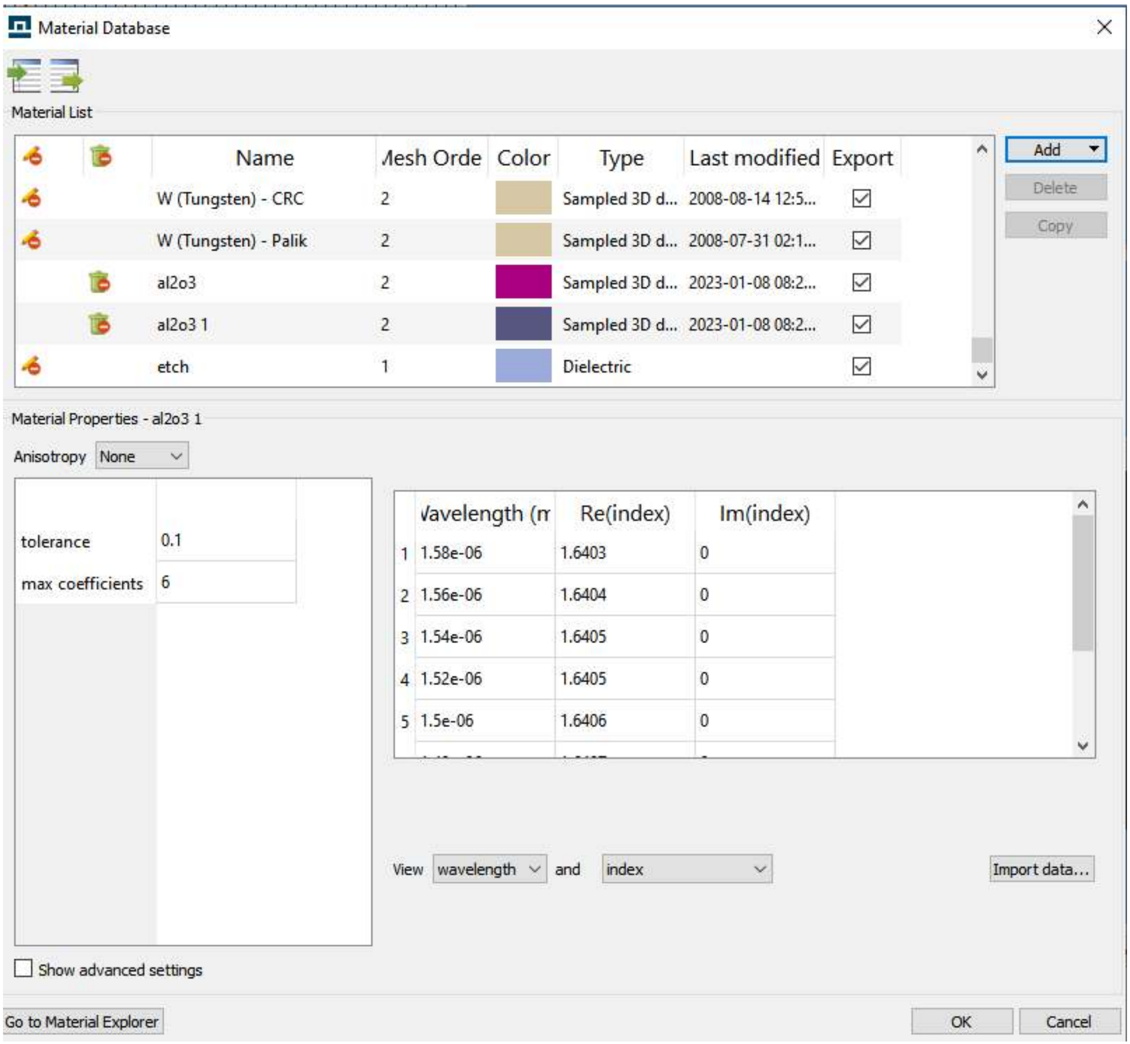

Figure 3.4. *Material library view, including externally added materials*

After adding the material, the geometries to be used are added by selecting them from the structure list. Within the "Structures" option, various geometries such as triangles, polygons, and circles are available, along with more complex structures like rings, waveguides, and surfaces. This wide range of options enables the construction and analysis of diverse geometrical configurations After the structure determines the geometry, its parameters are customized. In the Edit Window, the starting points and dimensions of the geometry on the X, Y, and Z axes are selected. Moreover, it can be chosen in width, height, sidewall angle, and pole settings. In addition to settings such as material, and name selection, detailed parameters such as rotations and graphical rendering can be arranged (Figure 3.5).

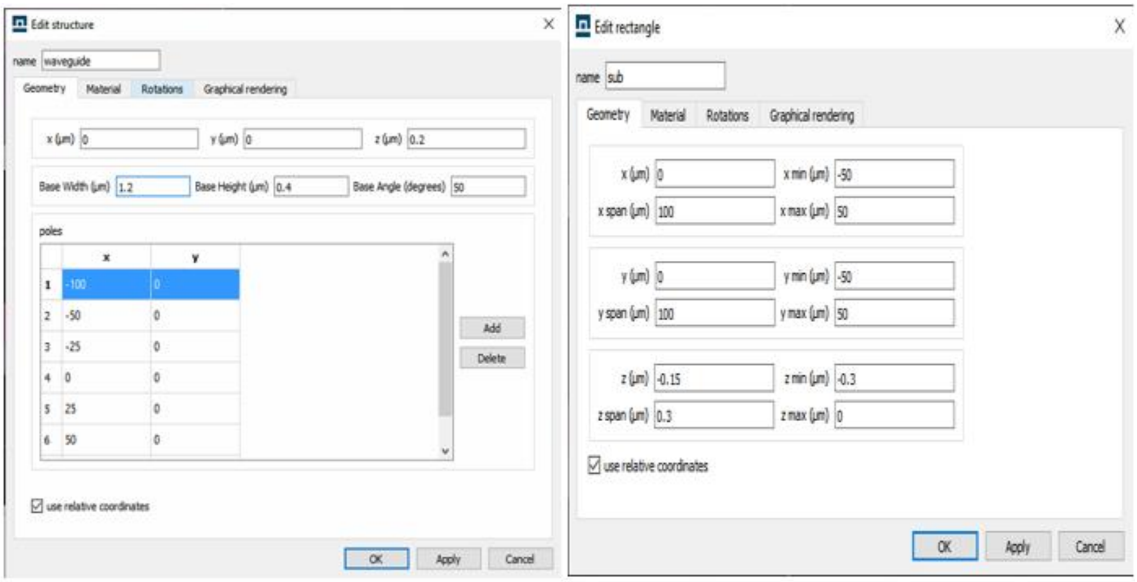

(a) (b)

Figure 3.5. *Example of waveguide (a) and rectangle (b) edit windows for editing structures to be used for simulation*

After adding the geometries, adjusting the parameters, and creating the structure to be simulated, one of the simulation solvers mentioned in the previous sections should be added. This is a must to get results from the simulation. In this simulation where modes are detected, the Eigenmode Solver named Finite Difference Eigenmode (FDE) is used. For the accuracy of the simulation results, the parameters that should be selected most accurately in the program are the solver parameters (Figure 3.6). First, the simulation temperature and background material should be chosen from the general section. Secondly, the required dimensions should be set in the geometry section. Height and width are significant when determining the simulation region. If a small region is selected, the results will be inaccurate due to boundary conditions. When a very large area is determined, it will be included in the simulation in leakage modes, and the simulation time will be unnecessarily long. It is always recommended to have two units from the bottom and three units from the top as height. The essential parameters of solvents are mesh settings and boundary conditions. Considering what has been explained in the previous sections, the most suitable boundary condition for this simulation is the Perfectly Match Layer (PML). The best solver geometry can be decided by performing several analyzes and evaluating the results.

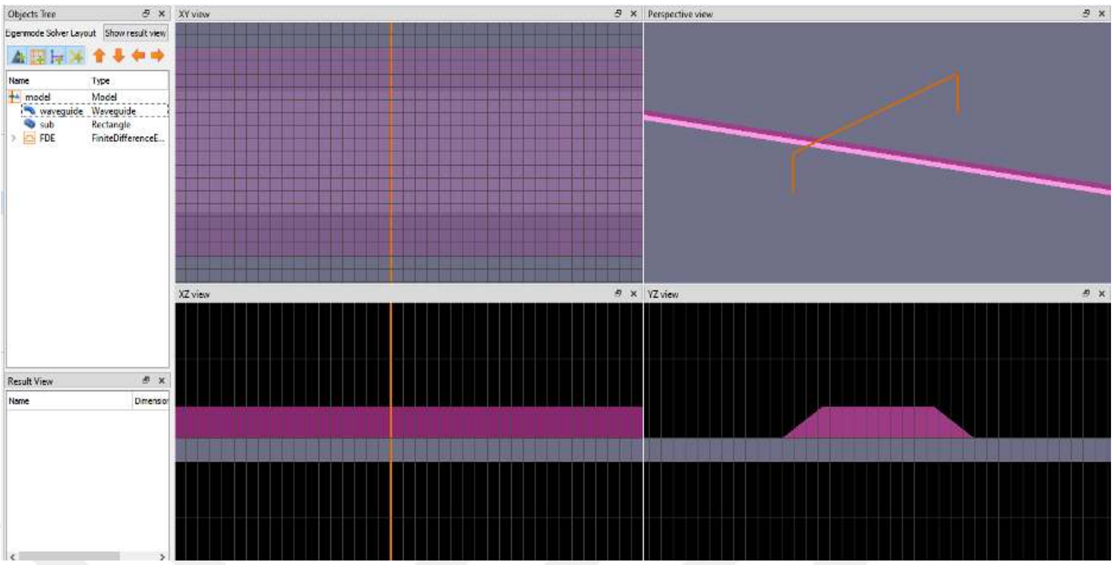

Figure 3.6. *The designed ridge waveguide prepared for simulation*

After adding all the necessary elements and setting the parameters, the simulation is run. In order to obtain the mode results, the Eigensolver Analysis Window must be used. According to the analysis, the values under the modal analysis, frequency analysis, or overlap analysis tabs should be filled. First, the correctness of the solver settings can be determined by pressing the mesh structure button. Different colors, such as yellow and blue, will be observed around the structure when the wrong dimensions are set. When observing colors and pixelated structures, it is imperative to readjust the solver settings. Rectifying this issue, arising from the width, height, and resolution of the simulation window, is crucial for obtain accurate analyses. A correct mesh structure is shown in Figure 3.7. A second point of choice is the shape of the waveguide. If a linear structure is used, there is no need to make any changes. However, the bent waveguide option and the bend radius should be selected for a bending waveguide analysis. This is important for the analysis result. Because the models supported by straight and bend waveguides with the same cross-section are different, one may be single mode while the other may be multimode or not support any mode. After these settings, mode calculations can be started by using the Calculate Modes button.

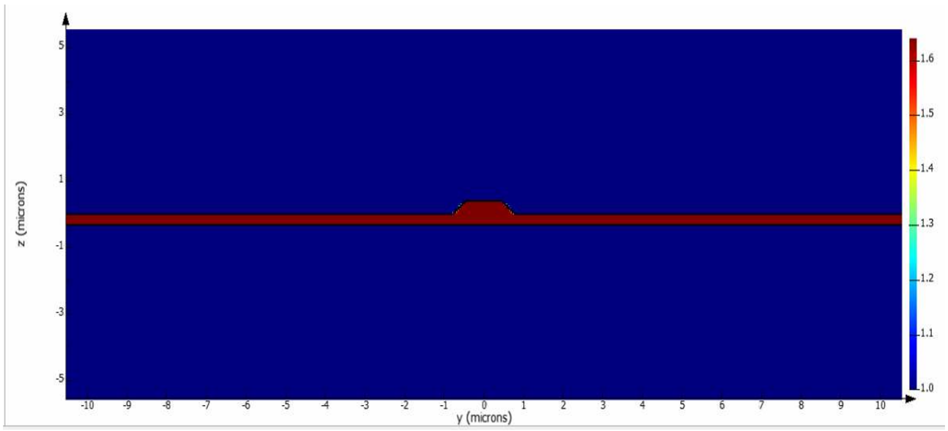

Figure 3.7. *Example of a suitable mesh structure*

3.2.1.2. Using the sweep function to detect the single-mode region

The waveguide is intended to be a single-mode waveguide. Lumerical has a software language that can make more advanced operations or prepare simulations more easily. This language, called Lumerical Script Language, has been used frequently in the simulations of the thesis. This language is essential, especially for determining the single-mode region. A sweep simulation was created using the Lumerical Script Language. Regions between specific sizes have been simulated in as small as 0.1-micrometer intervals. As a result of this simulation, the values in Figure 3.8 were obtained. The X-axis represents the etch depth thickness, the Y-axis the total thickness, and the Z-axis the waveguide width. Etch depth and total thickness was simulated between 0 and 1 µm, and waveguide width between 1 and 4 µm. Values greater than this do not support a single mode and are unsuitable for MOEMS devices. Purple dots are dimensions that support single mode. The star defines the multimode region. In non-mark sizes, no mods are supported. The three-dimensional graphic representation of the obtained data allows us to identify the single mode region. The simulation results enable us to make informed decisions regarding the dimensional range that needs to be maintained during the fabrication process. By using the results of the simulation, the right dimension intervals can be chosen and improve the fabrication processes.

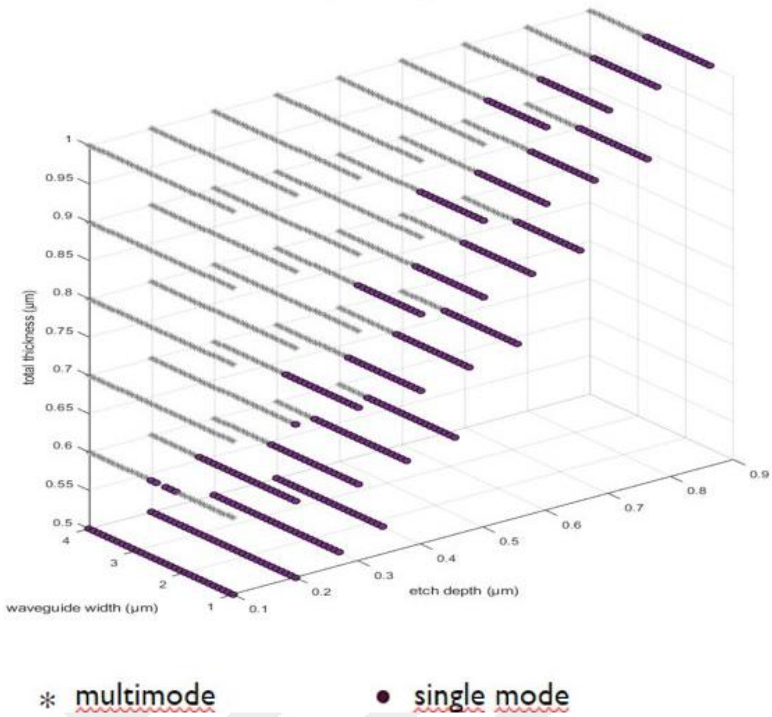

Figure 3.8. *Simulation results of single mode region of Al_2O_3 based ridge waveguide. Dots indicate single-mode sizes, stars indicate multimode sizes.*

To be more understandable, the graphics have been made two-dimensional by keeping the total thickness constant. Figure 3.9 shows the waveguide result with a total thickness of 0.7 µm; Figure 3.10 shows the waveguide result with a total thickness of 0.8 µm; and Figure 3.11 shows the waveguide result with a total thickness of 0.9 µm. The X-axis is the etch depth dimension; the Y-axis is the waveguide width. As in the previous chart, the dots are the single mode size, and the stars are the multimode size. Due to its ability to yield optimal results, provide mechanical robustness, and exhibit compatibility with fabrication methods, particular emphasis has been placed on the dimensions of 0.7 µm, 0.8 µm, and 0.9 µm. Notably, the most favorable and significant outcomes have been achieved with a total thickness of 0.7 µm. Upon completion of the design, it has been determined, based on the simulation results and calculations, that the optimal total thickness value is 0.7 µm. The data, transformed into a two-dimensional graph, has become highly readable, facilitating comprehensive analysis within the design.

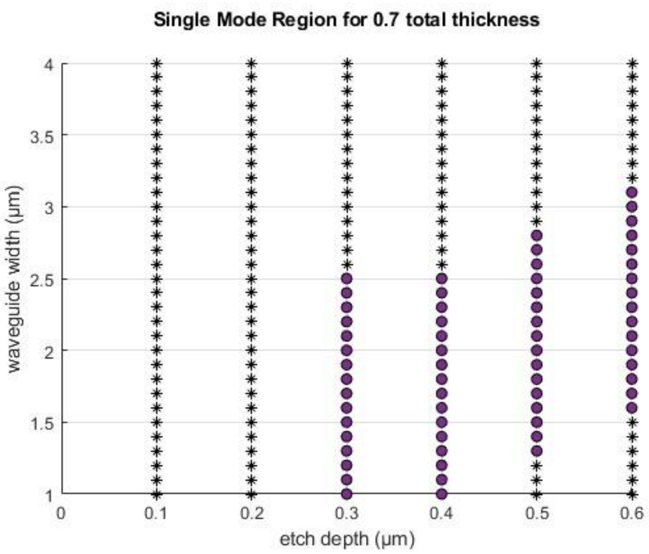

Figure 3.9. *Single mode region for a total thickness of 0.7 μm*

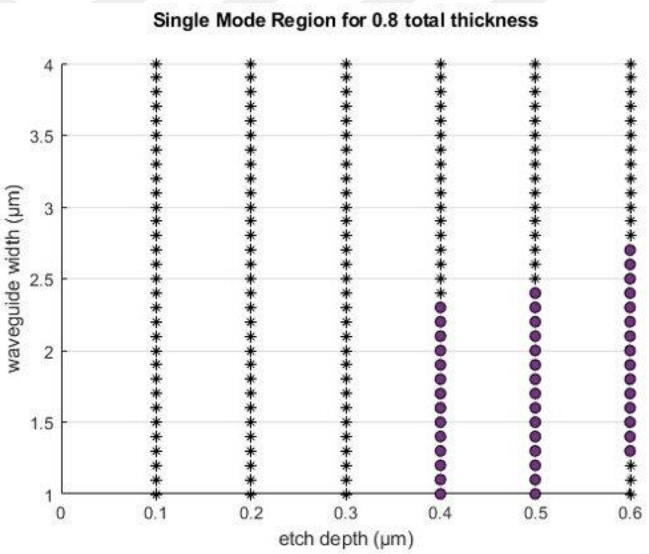

Figure 3.10. *Single mode region for a total thickness of 0.8 μm*

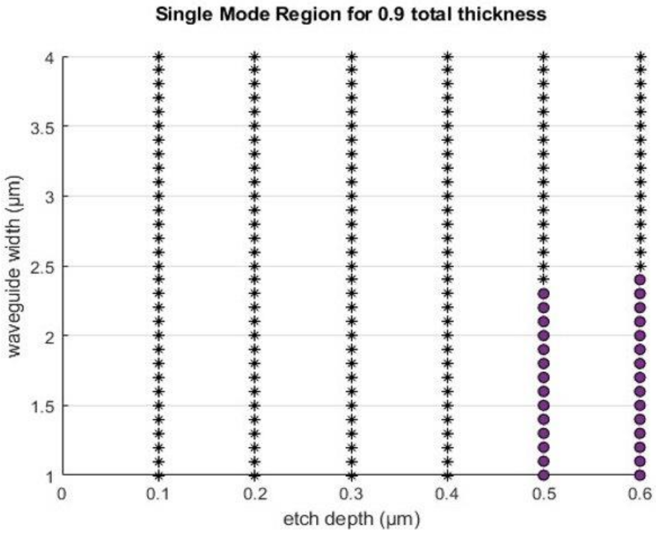

Figure 3.11. *Single mode region for a total thickness of 0.9 μm*

3.2.1.3. Simulation Results

TE mode with a total thickness of 0.7 micrometers and an etch depth of 0.3 micrometers is shown in Figure 3.12. According to the simulation results, the total thickness was 0.5 and 1 micrometers, the etch depth was 0.3 and 0.6 micrometers, and the waveguide width was between 1 and 2.4 micrometers. The results are also listed in Table 2.2. Identifying a cross-section in the middle of this range is essential to minimize fabrication errors and to remain in single mode as intended.

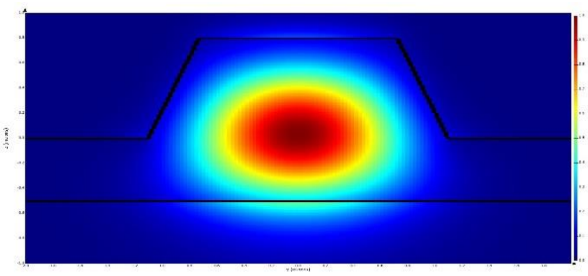

Figure 3.12. *Supported single mode for bus waveguide*

Table 3.2. *Single mode fabrication range for Al_2O_3-SiO_2 ridge waveguide*

parameter	Min value	Max value
e	0.3 μm	0.6 μm
t	0.5 μm	1 μm
w	1 μm	2.4 μm

4. RING RESONATOR

Ring resonators are integrated optical circuits. Depending on the design, it consists of different numbers of straight waveguides and rings. Ring resonators work with the wave sent from the input port circulating in a closed loop. Phase accumulation occurs due to interference in the wave circulating in the ring. Detection or sensing systems are created with the data obtained from the output, which is accepted as the output port. Since the desired waves are propagated in ring resonators, it acts as a notch filter. There is a coupling between the bus waveguide and the ring via wave evanescent or Multimode Interference (MMI). This study will focus on coupling by evanescent field.

4.1. Analysis Of Ring Resonators

Certain parameters are critical in the analysis of the ring resonator. The ring radius and the gap between the bus waveguide and the ring resonator are two parameters that significantly affect the results. Figure 4.1 shows a single mode ring resonator structure. E_{in} and E_{out} indicate the energy entering and leaving the ridge waveguide, respectively. The E_{r1} and E_{r2} represent the electric field of the incident waves coupled with the ring. t indicates the transmission coefficient, and κ indicates the coupling coefficient. R is the radius of the ring resonator, and α is the attenuation constant.

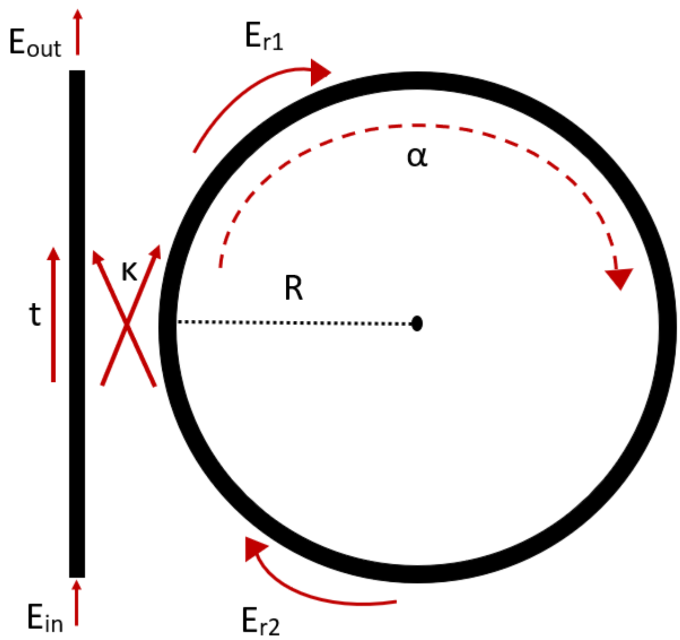

Figure 4.1. *Single Ring Resonator Structure and parameters (one bus-one ring)*

The sum of the transmission coefficient and coupling coefficient squares equals one. Eq. (3.1)

$$| t^2 | + | \kappa^2 | = 1 \tag{3.1}$$

The relationship between the energies of the fields and the coefficients is given as a matrix equation as follows:

$$\begin{pmatrix} E_{out} \\ E_{r1} \end{pmatrix} = \begin{pmatrix} t & k \\ -k^* & t^* \end{pmatrix} \begin{pmatrix} E_{in} \\ E_{r2} \end{pmatrix} \tag{3.2}$$

The formula for the accumulating phase is as follows:

$$\theta = \frac{2\pi L n_{eff}}{\lambda} \tag{3.3}$$

L represents the circumference of the ring, and L=2πR. n_{eff} is the effective refractive index of the material used. λ is the wavelength studied. a indicates the total losses. The loss coefficient, expressed as α, is calculated using the total loss.

$$\alpha = 10^{\frac{-aL}{20}} \tag{3.4}$$

There must be α=|t| for a critical coupling condition. Thus, the gap between the bus waveguide and the ring can be determined. The input and output wave energies can be calculated by the equation:

$$E_{out} = E_{in} \frac{-\alpha + t e^{-j\theta}}{-\alpha t^* + e^{-j\theta}} \tag{3.5}$$

The power transmission function of the system is calculated by this equation:

$$T = \left|{E_{out}}^2\right| = \frac{\alpha^2+|t|^2-2\alpha|t|\cos(\theta+\varphi)}{1+\alpha^2|t|^2-2\alpha|t|\cos(\theta+\varphi)} \tag{3.6}$$

The transmission function of the ring resonator is essential. The graph of this function gives information about important parameters such as the system's sensitivity. Values such as resonant wavelengths, Free Spectral Range (FSR), Full Width at Half Maximum (FWHM), Extinction Ratio (ER), Quality Factor (Q), and Finesse (F) can be obtained from this graph. A group index n_g is needed to calculate these parameters. This value can be obtained from the simulation results or calculated with the given equation:

$$n_g = n_{eff} - \lambda\frac{dn_{eff}}{d\lambda} \tag{3.7}$$

FSR is the wavelength difference between sequential resonances. The FSR value is expected to be wide and the FWHM value to be narrow.

$$FSR = \frac{\lambda^2}{n_g L} \tag{3.8}$$

$$FWHM = \frac{(1-\alpha|t|)\lambda^2}{\pi n_g L\sqrt{\alpha|t|}} \tag{3.9}$$

The ratio of the two values gives the F value. The F and Q values determine the sharpness of the function. In other words, since the Q value gives the stored energy and loss rate in each cycle, it is directly related to the efficient operation of the system.

$$F = \frac{FSR}{FWHM} \tag{3.10}$$

$$Q = \frac{\lambda}{FWHM} \tag{3.11}$$

ER is the ratio of the maximum and minimum power transmitted. The closer this value is to one, the better. ER=1, in case of the critical coupling condition .

$$ER = \frac{T_{max}}{T_{min}} = \left(\frac{(\alpha+|t|)(1-\alpha|t|)}{(\alpha-|t|)(1+\alpha|t|)}\right)^2 \quad (3.12)$$

4.2. Design Of Ring Resonator Based On Al_2O_3

A single mode Al_2O_3-based ring resonator is designed. In this design, a bus and ring waveguide is used. In the design, it is aimed to fully etch the ring resonator, leaving only Al_2O_3 material. It is planned to increase the sensitivity in the sensor application by completely etching the bottom of the ring. The structure of the bus waveguide consists of Al_2O_3 and SiO_2. The cross-sectional area of these structures is shown in Figure 4.2. Figure 4.2.a shows the cross-sectional area of the bus waveguide structure, and Figure 4.2.b shows the cross-sectional area of the ring resonator.

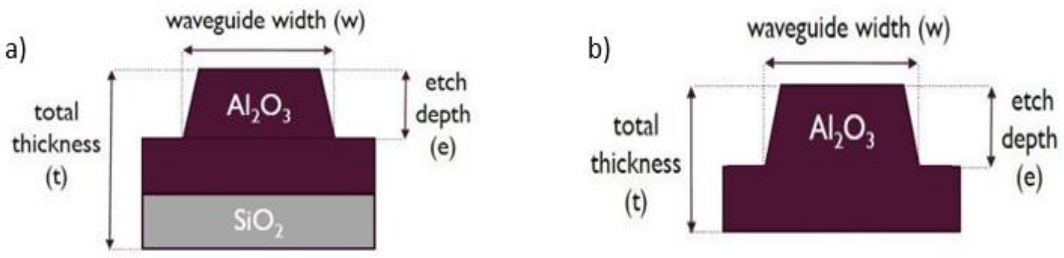

Figure 4.2. *Representation of the cross-sectional areas of the ring resonator. Al_2O_3-SiO_2 bus waveguide (a), Al_2O_3 ring resonator (b)*

The ridge waveguide results required for the bus waveguide structure of the single-ring resonator were discussed in detail in the previous section. However, new simulation results are necessary because the targeted structure for the ring resonator does not contain SiO_2 and is not straight but bent waveguide. The following chapters include work on the simulation of this new structure. The ridge waveguide will be used again for the ring structure. Due to the fabrication processes mentioned in the previous section, the wall angle was chosen as 50° . Since the ring was also desired to operate in the single mode region, simulations were made for the single mode region, and the safe fabrication region was determined. It is aimed to provide ease of fabrication by defining the common dimensions of the ridge waveguide containing SiO_2 and the ridge waveguide without it. In addition, while determining the radius of the ring resonator, the decision was made by analyzing the theoretical calculations and simulation results.

4.2.1. Simulation of the ring resonator

4.2.1.1. Preparations for simulation

In this study, a ring resonator consisting of one bus and one ring structure is designed. The ridge waveguide designed in the previous section is used for the bus structure. These dimensions fall within the ranges of 0.3 µm - 0.6 µm for etch depth, 0.5 µm - 1 µm for total thickness, and 1 µm - 2.4 µm for width. A similar structure will be used for the ring structure, but it was decided to etch the SiO_2 substrate to increase the sensitivity completely. In this case, the cross-sectional area of the ring structure was as shown in Figure 4.3. New simulations were required for the ring resonator to operate in single mode and for coupling the two to each other. In Chapter 3, the simulations for the Al_2O_3-SiO_2 structure are repeated using only Al_2O_3 material.

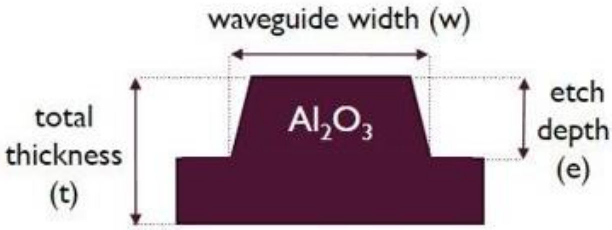

Figure 4.3. *Al_2O_3-based ridge waveguide cross-section.*

To find the range where the ring operates in single mode, the simulations in Chapter 3 were repeated using Al_2O_3 material only. However, since our structure was not straight this time, bend waveguide analysis was performed during the simulations. The range of dimensions that support the single mode in bend waveguides is narrower. When considering the integration of the one bus and one ring structures, this circumstance narrows the range of fabrication dimensions. Single mode region was determined by scanning the total thickness, etch depth, and waveguide thicknesses at 0.1-micrometer intervals. Figure 4.4 shows the single-mode operating region of the full etch Al_2O_3 structure. In this figure, where the data is visualized in a three-dimensional graph, the X-axis represents the etch depth, the Y-axis represents the total thickness, and the Z-axis represents the width of the ring resonator, similar to previous studies conducted.

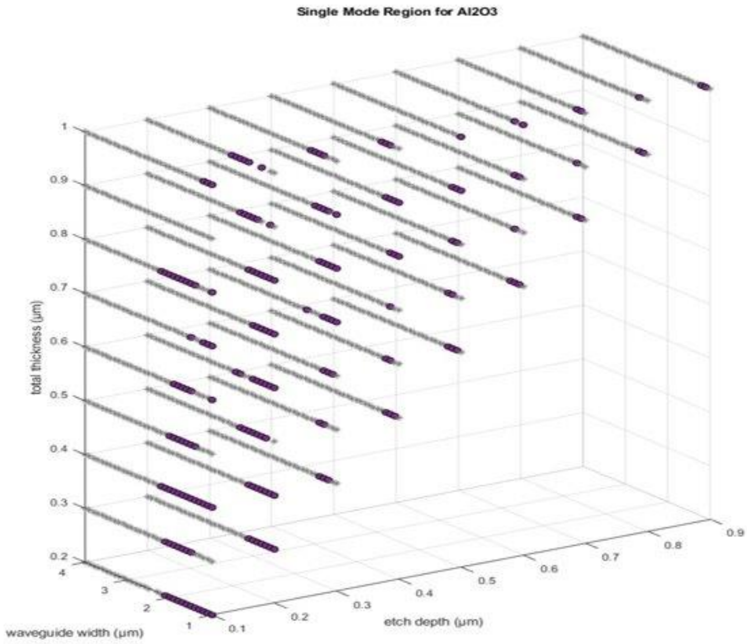

Figure 4.4. *Simulation results of single mode region of Al_2O_3 based bend waveguide. Dots indicate single-mode sizes, stars indicate multimode sizes.*

In order to be more understandable, the three-axis graph has been made biaxial by keeping the total thickness constant. The X-axis shows etch depth, and the Y-axis shows waveguide thickness. Figure 4.5 includes the results for a total thickness of 0.7 micrometers, Figure 4.6 for a total thickness of 0.8 micrometers, and Figure 4.7 for a total thickness of 0.9 micrometers. The dots indicate the single-mode cross-section, the stars are the multimode cross-section, and the blank areas are the regions where the mode is not supported.

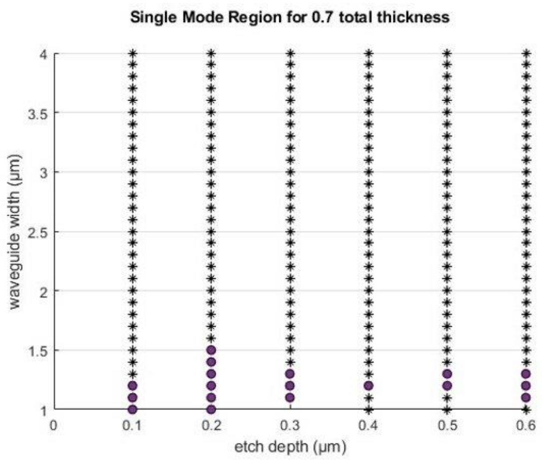

Figure 4.5. *Single mode region for a total thickness of 0.7 µm*

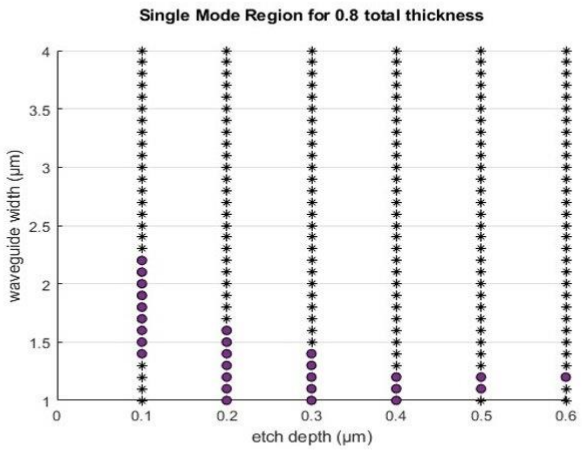

Figure 4.6. *Single mode region for a total thickness of 0.8 μm*

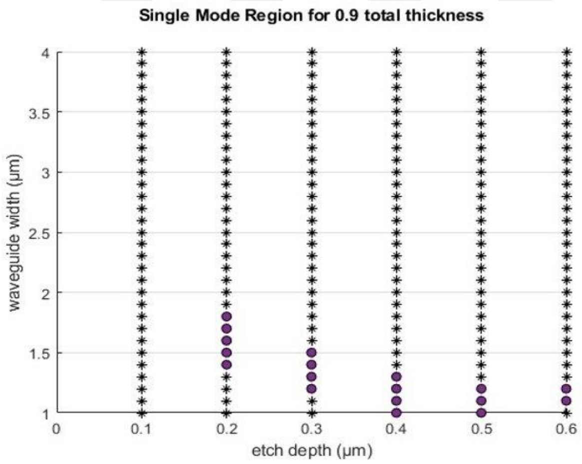

Figure 4.7. *Single mode region for a total thickness of 0.9 μm*

When the results of the simulations were analyzed, the safe single-mode region for fabrication was determined. According to the results, the etch depth was defined as 0.3 µm and 0.6 µm, the total thickness was 0.2 and 1 µm, and the waveguide thickness was between 1 and 1.3 µm. The results are listed in Table 4.1.

Table 4.1. *Single mode fabrication range for Al_2O_3 bend waveguide*

Parameters	Min value	Max value
e	0.3 µm	0.6 µm
t	0.2 µm	1 µm
w	1 µm	1.3 µm

Figure 4.8 includes the results for a common total thickness of 0.7 micrometers, Figure 4.9 for a common total thickness of 0.8 micrometers, and Figure 4.10 for a common total thickness of 0.9 micrometers. The blue dots in the two-dimensional graph represent the shared single mode region dimensions for both straight waveguides and bend waveguides. These common points are crucial in determining the dimensions as the structures are intended to be integrated during fabrication.

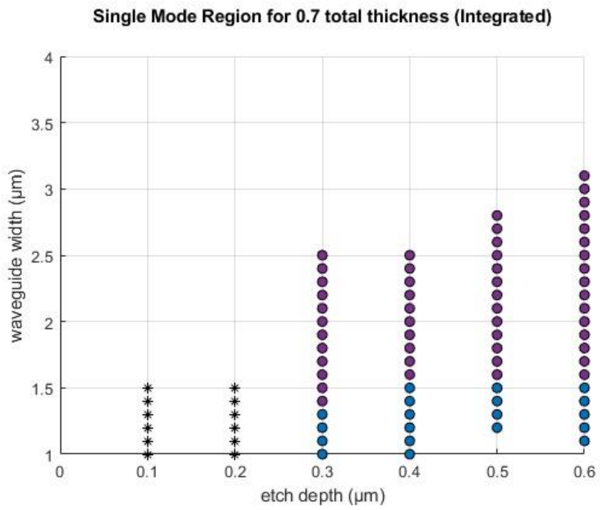

Figure 4.8. *Common single mode region for a total thickness of 0.7 microns*

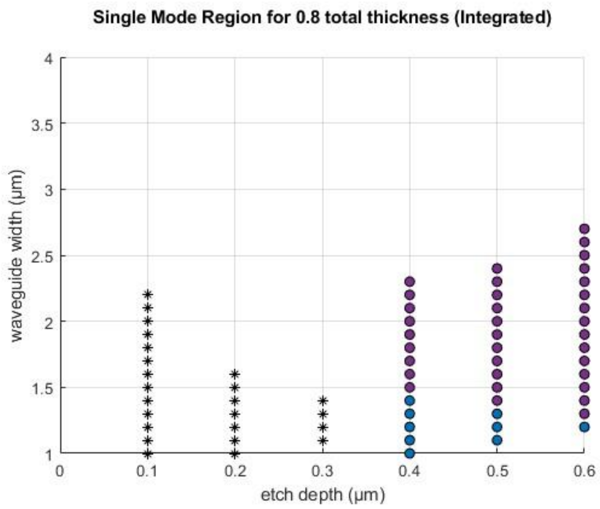

Figure 4.9. *Common single mode region for a total thickness of 0.8 microns*

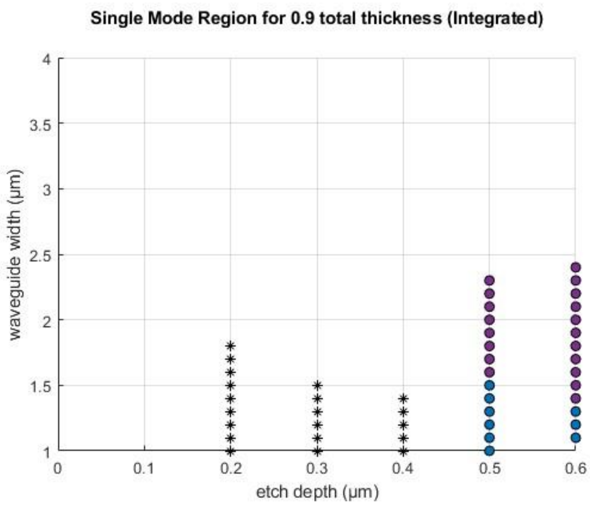

Figure 4.10. *Common single mode region for a total thickness of 0.9 microns*

In order to integrate the two structures and facilitate fabrication, the common ranges of the single mode were determined according to the simulation data. These results are listed in Table 4.2. From these values, 0.7 total µm thickness, 0.3 µm etch depth, and 1.2 µm waveguide width were selected.

Table 4.2. *The common single mode fabrication range for the Al_2O_3 waveguide and ring resonator*

Parameters	Min value	Max value
e	0.3 µm	0.6 µm
t	0.5 µm	1 µm
w	1 µm	1.5 µm

The cross-sectional area of the waveguide and ring resonator, the dimensions of which have been decided, integrated into Ansys Lumerical, and ready for simulation, is shown in Figure 4.11. The waveguide on the right is the bus waveguide and consists of Al_2O_3 and SiO_2 materials. The one on the left is the ring resonator, consisting of only Al_2O_3 material. The ring resonator, which is entirely made of fully etched Al_2O_3, has a suspended construction as seen in the figure. In contrast, the bus waveguide remains in a stationary position within the design.

Figure 4.11. *Ring resonator cross section in Ansys Lumerical.*

4.2.1.2. Using the sweep function to determine parameters

A single-mode ring resonator is defined in the cross-sectional area at the determined values. The gap value is significant for critical coupling. To find this value, a program was written with Lumerical script language. The transmission coefficient-coupling coefficient graph in Figure 4.12 was obtained by increasing the spacing between the ring and the waveguide in 0.01-micrometers intervals starting from 0.

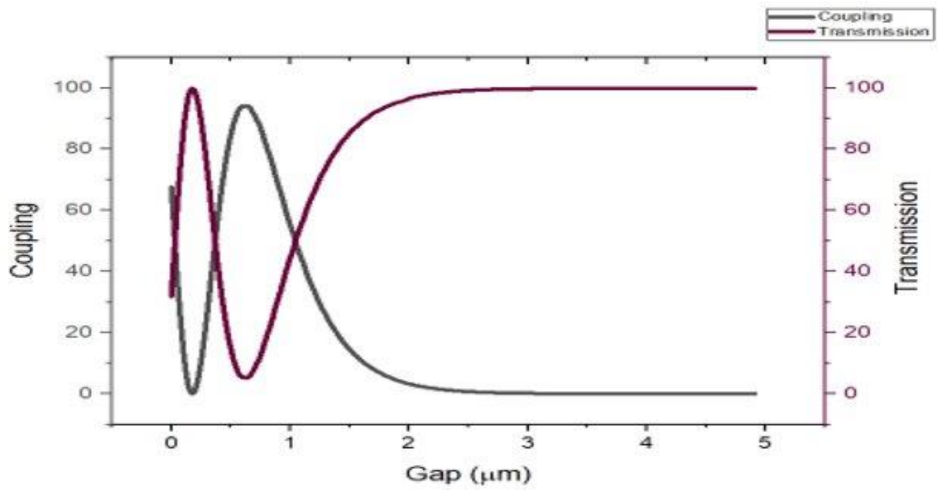

Figure 4.12. *Critical Coupling for ring resonator*

4.2.1.3. Simulation Results

The critical coupling gap is where the loss value and the transmission coefficient are equal and take the value of approximately 99.9. The critical coupling gap is one of the most important variables for the system to function properly. Applying the simulation to the entire design is unnecessary and leads to a significant waste of time. When a certain region of the ring resonator is simulated, and necessary calculations are made with the formulas given in the previous section, the critical coupling value is found as 1.3 micrometers. Figure 4.13 shows the simulated region, and figure 4.14 shows the coupling power. In the figure, it is clearly observed that the light source entering from the bus waveguide propagates along the ring resonator in a coupled manner, as evidenced by the calculated gap distance.

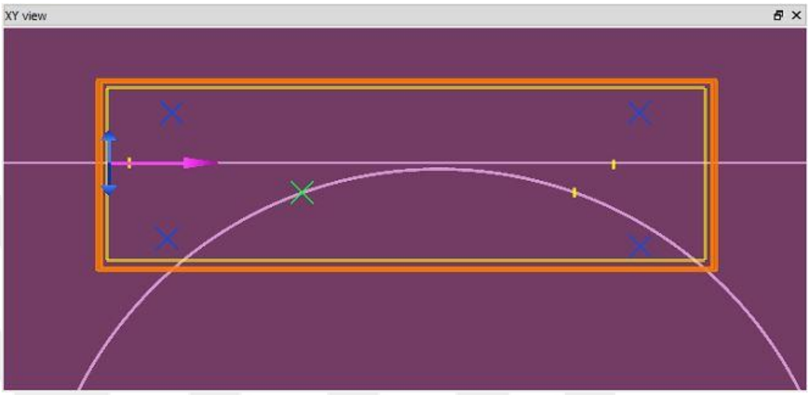

Figure 4.13. *Ring resonator coupling gap simulation top view in Ansys Lumerical*

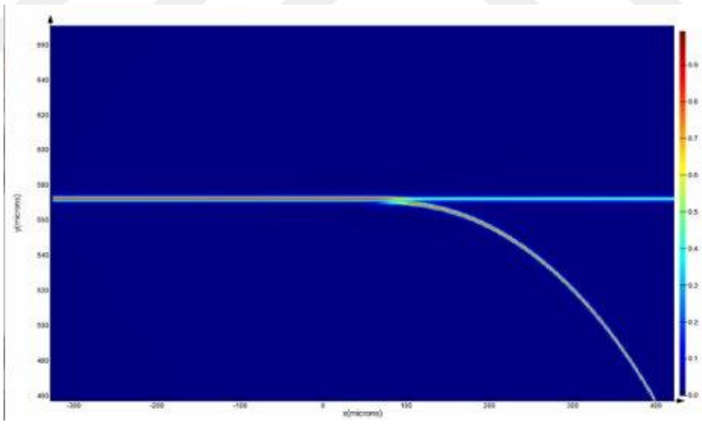

Figure 4.14. *Monitoring of power between ring resonator and waveguide at critical coupling gap*

The transmission spectrum obtained from the output port of the designed waveguide is given in Figure 4.15. Critical coupling resonant wavelengths are seen in the spectrum. These values in the graph are located either entirely or almost entirely at the point of convergence with zero. In the critical coupling condition, the wavelengths seen in the transmission spectrum are 1549.3 nm and 1549.85 nm, respectively.

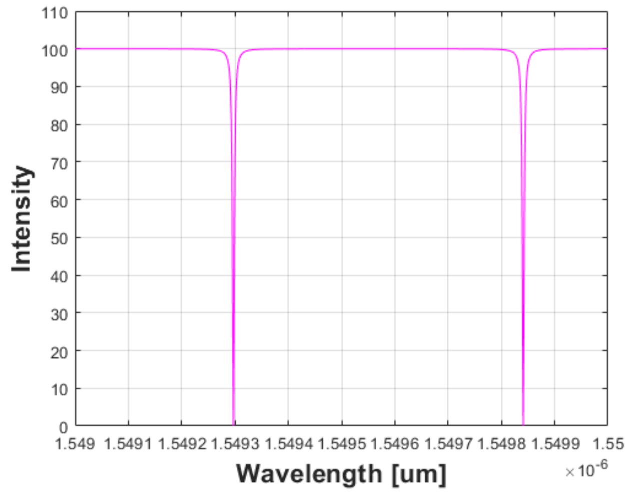

Figure 4.15. *Ring resonator transmission spectrum in critical coupling condition*

In addition, a wider spectrum was obtained by analyzing the wavelengths between 1545 nm and 1555 nm. In the spectrum in Figure 4.16, it is observed that every resonance wavelength can not reach zero. The fact that this value, called ER, is one hundred indicates that it is a critical coupling. All input waves propagate in the ring, and there is no transmission at the output port. The ER value is less than one hundred at wavelengths that are not fully coupled. From the ring resonator spectrum obtained, FSR 0.4468 nm, FWHM 3.0865 pm, F 144.762, and Q 5.0218 x 10^5 were found. The design results have wide FSR and narrow FWHM values as desired. Also, the resonances are sharp due to the F and Q values. The Q achieved at 10^5 times is a pretty good value compared to other designs in the market.

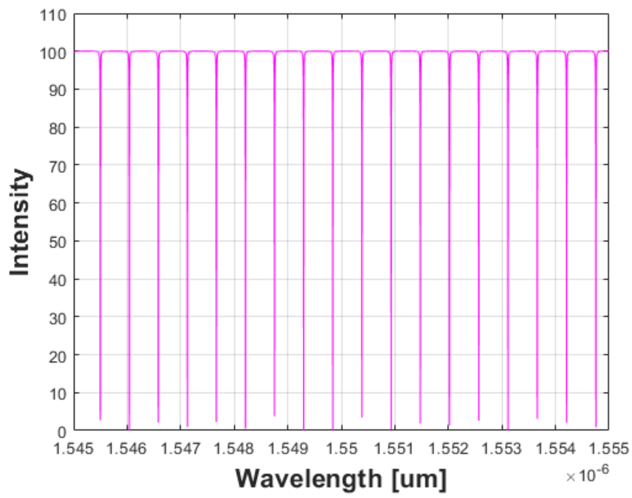

Figure 4.16. *Ring resonator transmission spectrum in wide wavelength range.*

5. CONCLUSION

In this thesis, studies on MOEMS accelerometer design and analysis were carried out. The device measures the shift in wavelength depending on the change in the refractive index. During the investigation, Ansys Lumerical Mode and Ansys Lumerical FDTD were used for optical simulations, Ansys Mechanical and Ansys Workbench were used for mechanical simulations, and Matlab software was used for necessary calculations and graphics.

The device was designed using a single-ring resonator. The ring resonator is placed on a cantilever with the ring structure suspended. When a force is applied to the device, or the device accelerates, the ring is bent. As a result of this bending, the refractive index of the material changes. Changing the refractive index causes a shift in the transmission spectrum by changing resonant wavelengths. The wavelength difference is measured and correlated with acceleration.

The width and length of the device are 1100 µm. Its thickness in the cantilever part is 0.7 µm. Full etch Al_2O_3 material is used in the cantilever part of the accelerometer. Al_2O_3 and SiO_2 are used in the supporting part. Mechanical simulations were made using boundary conditions and mesh methods for maximum accuracy. To increase the operating safety of the sensor, primarily resonance frequencies were found. After the resonance frequencies were determined, stress and deformation analyzes were performed. The displacement values observed as a result of the acceleration were calculated. This value was found to be a maximum of 2 micrometers at the very end of the cantilever.

A single-ring resonator consisting of a bus waveguide and a ring was used in the study. Since the device is desired to operate in the single mode region, the design parameters have been chosen considering this. Extensive simulations were performed with Lumerical to find the safe single-mode fabrication region. For the ridge waveguide structure, it is scanned between 0 µm and 1 µm in total thickness and between 0 µm and 4 µm in total waveguide width. These simulations were made separately with a full etch Al_2O_3 bending waveguide for the ring resonator and an Al_2O_3-SiO_2 structure for the bus waveguide. For the single mode region determined, common parameters have been found for ease of fabrication. As a result of the analysis, it was decided to use a ring resonator with a radius of 500 µm, considering the parameters such as loss and light confinement. The height of the ring resonator and the bus waveguide is 0.7 µm, and the width is 1.2

µm. It is aimed to prevent multimode support in case of possible fabrication errors by choosing these dimensions from the middle part of the determined single-mode window.

After simulating the optical and mechanical parts separately and analyzing the results, the results were combined to form the optomechanical structure. As a result of the object's acceleration, a wavelength shift of 0.982 nm was observed in the transmission spectrum. When these results were analyzed, it was observed that the waveguide losses of the sensor were 0.2±0.04 dB/cm, the optical sensitivity was 905 nm/RIU, and mechanical sensitivity was 0.11 nm/g. As compared in the previous sections, better results were obtained compared to similar structures.

Both micro ring resonator applications and the superior properties of Al_2O_3 material promise significant advantages for the future. Actual measurements can be tested by fabricating the accelerometer created in the following stages. As a result, improvements can be made to loss values and sensitivity. In addition, different sensor designs can be studied using the same ring resonator structure.

REFERENCES

Arnold, S. M., & Cole, B. E. (1988). Al2O3 A Films For Integrated Optıcs. In *Thin Solid Films* (Vol. 165).

Ay, F. (2005). *Silicon Based Dielectrics: Growth,Characterizatıon, And Applicatıons In Integrated Optics*. Ankara: Bilkent University, Instıtute of Engineering and Science.

Bhandarkar, S. (2005). Planar Waveguide Lasers. In B. D. Guenther & D. G. Steel (Eds.), *Encyclopedia of Modern Optics (Second Edition)* (Second Edition, pp. 384–393). Elsevier. https://doi.org/https://doi.org/10.1016/B978-0-12-809283-5.00851-X

Bonneville, D. B., Frankis, H. C., Wang, R., & Bradley, J. D. B. (2020). Erbium-ytterbium co-doped aluminium oxide waveguide amplifiers fabricated by reactive co-sputtering and wet chemical etching. *Optics Express*, *28*(20), 30130. https://doi.org/10.1364/oe.402802

Bradley, J. D. B. (Jonathan D. B., & Ipskamp). (2009). *Al2O3:ER3+ as a gain platform for integrated optics*. s.n.].

Bradley, J. D. B., Ay, F., Wörhoff, K., & Pollnau, M. (2007). Fabrication of low-loss channel waveguides in Al2O3 and Y2O3 layers by inductively coupled plasma reactive ion etching. *Applied Physics B: Lasers and Optics*, *89*(2–3), 311–318. https://doi.org/10.1007/s00340-007-2815-3

Bradley, J. D. B., Hosseini, E. S., Purnawirman, Su, Z., Adam, T. N., Leake, G., Coolbaugh, D., & Watts, M. R. (2014). Monolithic erbium- and ytterbium-doped microring lasers on silicon chips. *Optics Express*, *22*(10), 12226. https://doi.org/10.1364/oe.22.012226

Caballero-Espitia, D. L., Lizarraga-Medina, E. G., Borbon-Nuñez, H. A., Contreras-Lopez, O. E., Tiznado, H., & Marquez, H. (2020). Study of Al2O3 thin films by ALD using H2O and O3 as oxygen source for waveguide applications. *Optical Materials*, *109*. https://doi.org/10.1016/j.optmat.2020.110370

Chen, F., Xu, Q., Zhang, P., Zhang, Z.-B., Wong, W.-H., Pun, E. Y.-B., & Zhang, D.-L. (2019). Measurement of refractive index of powder by prism coupler. *Review of Scientific Instruments*, *90*(9). https://doi.org/10.1063/1.5110886

Chen, X., Zhou, J., Zhou, W., & Shen, W. (2007). Frame transfer CCD driving circuit design for space camera. *Electronic Imaging and Multimedia Technology V*, *6833*, 68331H. https://doi.org/10.1117/12.756652

Chen, Y., Li, Z., Yi, H., Zhou, Z., & Yu, J. (2009). Microring resonator for glucose sensing applications. *Frontiers of Optoelectronics in China*, *2*(3), 304–307. https://doi.org/10.1007/s12200-009-0047-3

Chiang, K. S. (2010). Development of optical polymer waveguide devices. *Optoelectronic Integrated Circuits XII*, *7605*, 760507. https://doi.org/10.1117/12.845575

De, A. sen, & Sen, U. (2011). *Quantum Advantage in Communication Networks*. http://arxiv.org/abs/1105.2412

De Goede, M., Dijkstra, M., Obregón, R., Ramón-Azcón, J., Martínez, E., Padilla, L., Mitjans, F., & Garcia-Blanco, S. M. (2019). Al 2 O 3 microring resonators for the detection of a cancer biomarker in undiluted urine . *Optics Express*, *27*(13), 18508. https://doi.org/10.1364/oe.27.018508

De Goede, M. (2020). *Sensing technologies on active and passive Al2O3 glass*. [PhD Thesis - Research UT, graduation UT, University of Twente]. University of Twente. https://doi.org/10.3990/1.9789036549660

Demirtas, M., Odaci, C., Perkgoz, N. K., Sevik, C., & Ay, F. (2018). Low Loss Atomic Layer Deposited Al2O3 Waveguides for Applications in On-Chip Optical Amplifiers. *IEEE Journal of Selected Topics in Quantum Electronics*, *24*(4). https://doi.org/10.1109/JSTQE.2018.2825880

Dianov, E. M. (2010). Fibre optics: Forty years later. *Quantum Electronics*, *40*(1), 1–6. https://doi.org/10.1070/QE2010v040n01ABEH014260

Dong, B., Cai, H., Tsai, J. M., Kwong, D. L., & Liu, A. Q. (2013). An on-chip opto-mechanical accelerometer. *2013 IEEE 26th International Conference on Micro Electro Mechanical Systems (MEMS)*, 641–644. https://doi.org/10.1109/MEMSYS.2013.6474323

Edlmayr, V., Moser, M., Walter, C., & Mitterer, C. (2010). Thermal Stability Of Sputtered Al2O3 Coatings. *Surface and Coatings Technology*, *204*(9–10), 1576–1581. https://doi.org/10.1016/j.surfcoat.2009.10.002

Hadi Kusuma, H., Saidin, M. K., & Ibrahim, Z. (2009). Optical Properties Of Ti:Al2O3 Sıngle Crystal. In *J. Fiz. UTM* (Vol. 4).

Il'inskii, A. S. (2019). Development of the Electromagnetic Theory of Radio Waveguides. In *Journal of Communications Technology and Electronics* (Vol. 64, Issue 8, pp. 723–728). Pleiades Publishing. https://doi.org/10.1134/S1064226919080060

Iwai, H., & Ohmi, S. N. ichiro. (2002). Silicon integrated circuit technology from past to future. *Microelectronics Reliability*, *42*(4–5). https://doi.org/10.1016/S0026-2714(02)00032-X

Kianisarkaleh, A., Lahijani, B., Saberkari, H., & Esmaeeli, A. (2017). Optical Ring Resonators: A Platform for Biological Sensing Applications. *Journal of Medical Signals & Sensors*, *7*, 185–191. https://doi.org/10.4103/jmss.JMSS_9_17

Kikuchi, K. (2010). Coherent Optical Communications: Historical Perspectives and Future Directions. In M. Nakazawa, K. Kikuchi, & T. Miyazaki (Eds.), *High Spectral Density Optical Communication Technologies* (pp. 11–49). Springer Berlin Heidelberg. https://doi.org/10.1007/978-3-642-10419-0_2

Kim, K. H., & Fan, X. (2015). Surface Sensitive Microfluidic Optomechanical Ring Resonator Sensors. *2015 Conference On Lasers And Electro-Optics (CLEO)*.

Kogelnik, H. (1988). Theory of Optical Waveguides. In T. Tamir (Ed.), *Guided-Wave Optoelectronics* (pp. 7–88). Springer Berlin Heidelberg. https://doi.org/10.1007/978-3-642-97074-0_2

Kumar, C., & Patel, N. (1992). Optoeleetronics-past, present, and futurC. In *Parts* (Vol. 17).

Kwon, M.-S., & Steier, W. H. (2008a). *Microring-resonator-based sensor measuring both the concentration and temperature of a solution*. http://www.rsoftinc.com.

Kwon, M.-S., & Steier, W. H. (2008b). Microring-resonator-based sensor measuring both the concentration and temperature of a solution. *Opt. Express*, *16*(13), 9372–9377. https://doi.org/10.1364/OE.16.009372

Li, N., Magden, E. S., Su, Z., Singh, N., Ruocco, A., Xin, M., Byrd, M., Callahan, P. T., Bradley, J. D. B., Baiocco, C., Vermeulen, D., & Watts, M. R. (2018). Broadband 2-µm emission on silicon chips: monolithically integrated Holmium lasers. *Optics Express*, *26*(3), 2220. https://doi.org/10.1364/oe.26.002220

Li, Y., Liang, J., Zhang, Q., Zhou, Z., Li, H., Fan, X., Wang, X., Fan, P., Yang, Y., Guo, P., Zhuang, X., Zhu, X., Liao, L., & Pan, A. (2015). Optical waveguide beam splitters based on hybrid metal-dielectric-semiconductor nanostructures. *Optics Communications*, *354*, 168–173. https://doi.org/10.1016/j.optcom.2015.05.058

Liu, X., Xue, C., Van, S., Xiong, J., & Zhang, W. (2009). Integrated high sensitivity displacement sensor based on micro ring resonator. *4th IEEE International Conference on Nano/Micro Engineered and Molecular Systems, NEMS 2009*, 1000–1003. https://doi.org/10.1109/NEMS.2009.5068742

Mounier, E., de Charentenay, Y., & Eloy, J.-C. (2006). New applications for MOEMS. In H. Urey, D. L. Dickensheets, & B. P. Gogoi (Eds.), *MOEMS Display, Imaging, And Miniaturized Microsystems IV* (Vol. 6114). https://doi.org/10.1117/12.634755

NASA, (2022). https://science.nasa.gov/technology/technology-highlights/high-efficiency-charge-coupled-devices-enable-on-sky-observations (Date accessed: 12.12.2022)

Pathak, P. H., Feng, X., Hu, P., & Mohapatra, P. (2015). Visible Light Communication, Networking, and Sensing: A Survey, Potential and Challenges. *IEEE Communications Surveys & Tutorials*, *17*(4), 2047–2077. https://doi.org/10.1109/COMST.2015.2476474

Piprek, J. (2017). Introduction to Optoelectronic Device Principles. In S. S. Sun & L. R. Dalton (Eds.), *Introduction to Organic Electronic And Optoelectronic Materials And Devices, 2nd Edition.*

Pollock, C. R., & Lipson, M. (2003). *Integrated Photonics*. Springer US. https://doi.org/10.1007/978-1-4757-5522-0

Schaller, R. R. (1997). Moore's law: past, present and future. *IEEE Spectrum*, *34*(6), 52–59. https://doi.org/10.1109/6.591665

Schwertz, K., & Burge, J. H. (1988). *Optomechanical Design and Analysis Field Guide to Downloaded From: http://ebooks.spiedigitallibrary.org/ on 12/04/2012 Terms of Use: http://spiedl.org/terms*. http://spiedl.org/terms

Selvarajan, A. (1992). *Integrated optics-technology and applications* (Vol. 17).

Singha, S., & Bhowmik, B. B. (2018). On-chip Photonic Temperature Sensor Using Micro Ring Resonator. *2018 Fifteenth International Conference on Wireless and Optical Communications Networks (WOCN)*, 1–4. https://doi.org/10.1109/WOCN.2018.8556121

Su, Z., Li, N., Salih Magden, E., Byrd, M., Purnawirman, Adam, T. N., Leake, G., Coolbaugh, D., Bradley, J. D. B., & Watts, M. R. (2016). Ultra-compact and low-threshold thulium microcavity lasermonolithically integrated on silicon. *Optics Letters*, *41*(24), 5708–5711. https://doi.org/10.1364/OL.41.005708

Vera, F., Rivera, R., & Ortíz, M. (2014). A simple experiment to measure the inverse square law of light in daylight conditions. *European Journal of Physics*, *35*(1). https://doi.org/10.1088/0143-0807/35/1/015015

Yang, J., & Guo, L. J. (2006). Optical sensors based on active microcavities. *IEEE Journal on Selected Topics in Quantum Electronics*, *12*(1), 143–147. https://doi.org/10.1109/JSTQE.2005.862953

Zhang, L., Agarwal, A. M., Kimerling, L. C., & Michel, J. (2014). Nonlinear Group IV photonics based on silicon and germanium: From near-infrared to mid-infrared. In *Nanophotonics* (Vol. 3, Issues 4–5, pp. 247–268). Walter de Gruyter GmbH. https://doi.org/10.1515/nanoph-2013-0020

Zhang, Q. Y., Wang, P. S., Zhao, W. J., & Wang, L. (2000). Ion beam assisted deposition of Al O optical waveguides on 2 3 silicon. In *Surface and Coatings Technology* (Vol. 128129).

CURRICULUM VITAE

ORCID ID: 0000-0002-0204-2963

Name Surname : Safiye Yücel

Educational Background:

- 2023,Eskişehir Technical University / Electrical and Electronics Engineering / Electromagnetic Fields and Microwave Circuits (MSc)
- 2020, Eskişehir Osmangazi University /Electrical and Electronics Engineering (BSc)
- 2018, Anadolu University Open Education Faculty/Business Administration Department (BSc)

Work Experience:

- January 2020 – Present : Eskişehir Technical University
  Researcher (Micro-Nano Devices and Systems Laboratory)
- February 2022 - Present : Tubitak - Turkish Technology Team
  Deneyap Türkiye Aviation and Space Technologies Instructor
  Deneyap Türkiye Robotic and Coding Instructor
  Deneyap Türkiye Mobile Application Instructor
  Deneyap Türkiye Artificial Intelligence Instructor
  Deneyap Türkiye Energy Technologies Instructor
- February 2020-June 2020 : Tubitak - Turkish Technology Team
  Deneyap Türkiye Electronic Programming and Internet of Things Instructor
- December 2019-January 2020 : Eltagron Electronic
  Intern Engineer
- Eylül 2019-Ocak 2020 : Tubitak - Turkish Technology Team
  Deneyap Türkiye Robotics and Coding Instructor
- August 2018-September 2018: Tronik Defence and Aviation
  Intern Engineer
- September 2017 - February2019: Eskişehir Osmangazi University
  Student Assistant (Circuit Analysis and Systems Laboratory)

Projects:

- Autonomous Metal Detector Robot
- Smart Refrigerator (Arçelik Second Place in Competition)
- Color Sorter Robot
- Smart Walking Stick
- Solar Phone Charging Station
- Electric Car

Non-Work Experience:

- IEEE ESOGÜ Alumni Interview Event Coordinator
- IEEE ESOGÜ Social Responsibility Projects Presidency
- TISP (Making Presentations to Students About Engineering and Project Studies)
- HoC (Teaching Students about Coding Languages)
- Social Responsibility Projects (Robot hand, intelligent walking stick, IEEE ESOGÜ Memorial Forest, Village School Restoration, Sign Language Education, and Video Preparation)

Foreign Language:

- English
- French
- German

Skills:

- Ansys Lumerical, Ansys Mechanical, C, C#, C++, Matlab, Proteus, CST, Python, TIA Portal, AutoCAD, MPLAB, Mission Planner, COMSOL Multiphysics, LEGO Mindstorms EV3, Gantt Project
- Microsoft Office (Word, Excel, PowerPoint, Visio)
- Arduino, Raspberry Pi, PLC
- Adobe Photoshop, Camtasia, Movie Maker

Certificate:

- Sign Language

Club and Association Membership:

- IEEE
- TEMA